

**Proceedings of the Institution of Mechanical Engineers- Part N:
Journal of Nanomaterials, Nanoengineering and Nanosystems**

eISSN: 23977922 | ISSN: 23977914

PUBLISHER: SAGE PUBLISHING

ACCEPTED MARCH 16TH 2017

FINITE ELEMENT COMPUTATION OF TRANSIENT DISSIPATIVE DOUBLE DIFFUSIVE MAGNETO-CONVECTIVE NANOFLUID FLOW FROM A ROTATING VERTICAL POROUS SURFACE IN POROUS MEDIA.

Thirupathi Thumma^{1*}, O. Anwar Bég² and Siva Reddy Sheri³

¹Department of Mathematics, B V Raju Institute of Technology, Medak, 502313, Telangana, India.

² Fluid Mechanics, Spray Research Group, Petroleum/Gas Engineering Division, Newton Bldg., University of Salford, Manchester, M54WT, UK.

³Department of Mathematics, Gandhi Institute of Technology/Management University, Hyderabad, India.

*Corresponding author-Email: thirupathi.thumma@gmail.com

Running head:

FINITE ELEMENT TRANSIENT DISSIPATIVE MAGNETO-CONVECTIVE NANOFLUID FLOW

Abstract:

This paper aimed to investigate the transient dissipative MHD double diffusive free convective boundary layer flow of electrically-conducting nanofluids from a stationary or moving vertical porous surface in a rotating high permeability porous medium, considering buoyancy, thermal radiation and first order chemical reaction. Thermo-diffusion (Soret) and diffuso-thermal (Dufour) effects are also considered. Darcy's law is employed. The mathematical model is formulated by considering water-based nanofluids containing metallic nano-particles for both stationary and moving plate cases. Three nanofluids are examined, namely copper, aluminium oxide or titanium oxide in water. The transformed non-linear, coupled, dimensionless partial differential equations describing the flow are solved with physically appropriate boundary conditions by using Galerkin weighted residual scheme. For prescribed permeability, numerical results are presented graphically for the influence of a number of emerging parameters. Validation of finite element solutions for skin friction and Nusselt number is achieved via comparison with the previously published work as special cases of the present investigation and very good correlation obtained. Increasing rotational parameter is observed to reduce both primary and secondary velocity components. Primary and secondary velocities are consistently elevated with increasing Soret, Dufour, thermal Grashof and solutal Grashof numbers. Increasing Schmidt number, chemical reaction and suction parameter both suppress nano - particle concentration whereas the converse behavior is computed with increasing Soret number. The study is relevant to high temperature rotating chemical engineering systems exploiting magnetized nanofluids and also electromagnetic nanomaterial manufacturing processes.

Keywords: *Double diffusive convection; Nanofluid; Rotating fluid; Buoyancy; Chemical reaction; Radiation.*

Introduction

Magnetic nanofluids are emerging as a new branch of possible working fluids with potential in, for example, electrical transformer technologies, medical engineering and fusion power systems. These fluids are manufactured by dispersing magnetic nanoparticles in base fluids e.g. water, and are responsive to the application of magnetic fields. To simulate the manufacture of such materials, magnetohydrodynamics provides an excellent platform. Additionally many stable magnetic nanofluids are synthesized at high temperatures and this invokes thermal radiative heat transfer (Zaid et al. [1]; Sergis et al. [2]). Recently, the study laminar 3 dimensional convection flow of Al_2O_3 -water bio-nanofluids in a circular tube under constant wall temperature conditions was simulated with FVM (Finite Volume Method) by Beg et al. [3] as well as flow past in wavy channel by adopting control volume approach investigated by Rashidi et al. [4]. Metallic nanoparticles have been shown to hold excellent features for radiation absorption due to the plasmon resonance absorption band in the visible and near IR spectrum that can be tuned by engineers to optimize properties. Other effects may also arise e.g. chemical reaction and rotation of systems (Borbath et al. [5]). In nuclear engineering implementation of magnetic nanofluids, many of these effects can also arise simultaneously. Furthermore the deployment of magnetic nano-particles in drug delivery may also benefit from investigations of chemically reactive magnetic nanofluids with rotational body forces. It is therefore of benefit to improving such designs and optimizing performance that continuous development in mathematical and computational models is sustained and refined. This motivates the present numerical investigation.

In recent years a number of investigations of magnetohydrodynamic nanofluid convection flows have been reported. These studies have extended the pioneering work into coolants of Choi at Argonne National Laboratory in the United States in the mid-1990s (Choi [6]; Choi et al. [7]) coined the term nanofluid to describe fluids engineered by suspending small volumetric nanoparticles ($Cu, Al, Al_2O_3, TiO_2, SiC, SiN, AlN$) with average sizes less than 100 nm in conventional heat transfer fluids ($H_2O, C_2H_6O_2$) and also other base fluids like engine oil, mineral oil, bio-fluids and poor heat transfer fluids. The thermal-enhancing properties of magnetic nanofluids have attracted increasing interest in ever-diversifying fields such as electronics, optical devices, material synthesis, high power x-rays, lasers and biomedical sciences. Most studies of magnetic nanofluid transport have utilized the Lorentz magnetic body force formulation. (Oztop et al. [8]) studied the hydromagnetic natural convection in an enclosure from two semi-circular heaters on the bottom wall. (Chamkha and Aly [9]) reported on magnetic free convective flow of a nanofluid with heat sink/source effects. (Ellahi [10]) studied the MHD flow of non-Newtonian nanofluid in a pipe. Recently, the fourth order Runge-Kutta Shooting technique is employed to investigate the unsteady MHD laminar convective nanofluid flow over permeable accelerated stretching vertical surface by Freidoonimehr et al. [11]. (Sheikholeslami et al. [12]) investigated magnetic field effects on nanofluid flow and heat transfer in a semi-annulus enclosure by considering the effects of thermophoresis and Brownian motion and evaluated the gradient of nanoparticles volume fraction.

Rotating flows of nanofluids have also garnered considerable attention. Such studies invoke Coriolis body force terms due to the rotation of the nanofluid. (Mahajan and Arora [13]) considered convective instability in a thin layer of a rotating magnetic nanofluid, considering Brownian diffusion, thermophoresis and magnetophoresis effects. Using a Chebyshev pseudo

spectral numerical method and considering different boundary conditions, they found that for water and ester based magnetic nanofluids, the magnetic field dominates the buoyancy mechanism in fluid layers about 1 mm thick. (Nadeem and Saleem [14]) investigated with a homotopy analysis method (HAM) the transient mixed magnetohydrodynamic rotating nanofluid convection on a rotating cone with magnetic field, and considered three different cases where the fluid is rotating and the cone is at rest, the fluid and the cone are rotating with equal angular velocity in the same direction and where only the cone is in rotation. They showed that magnetic field depresses velocity magnitudes and that velocity field is modified significantly depending on the rotation case employed. (Beg et al. [15]) analyzed the transient stagnation-point boundary layer flow of nanofluids from a spinning sphere, using both homotopy and Adomian decomposition methods. They showed that with increasing rotational parameter i.e. stronger swirl effect proportional to the rotational velocity of the sphere), primary velocity is enhanced whereas secondary velocity is reduced and also temperatures and nano-particle concentration magnitudes decreased. (Rana et al. [16]) studied with a variational finite element algorithm, the transient magneto-hydrodynamic boundary layer flow and heat transfer in an incompressible rotating nanofluid over a stretching continuous sheet, showing that both primary and secondary velocity are strongly retarded with increasing Hartmann (magnetic) number whereas temperature and nanoparticle concentration are enhanced. They also found that greater rotational parameter decelerates both primary and secondary velocity, and reduces temperature and nanoparticle concentration. (Sheikholeslami et al. [17]) used a fourth-order Runge–Kutta method to study magnetohydrodynamic (MHD) nanofluid flow and heat transfer in a rotating parallel plate channel system, considering copper, silver, alumina and titanium oxide nano-particles suspended in water. They showed that Nusselt number is a maximum for the titanium oxide-water nanofluid case whereas it is strongly reduced with increasing magnetic parameter. (Hamad and Pop [18]) also examined rotating hydromagnetic nanofluid convection from a permeable plate, noting that with increasing rotation and heat source parameters, the skin friction is reduced as is the temperature and thermal boundary layer thickness.

Chemical reaction and thermal radiative effects in nanofluid flows are, as elaborated earlier, also of interest, in particular during high-temperature synthesis of nano-particle suspensions. Usually a first order chemical reaction model is employed, although reactions may be more complex. They can be homogenous or heterogeneous and also may be of second or higher order. Interesting studies of chemically-reacting nanofluid flows (with magnetohydrodynamics) have appeared quite recently in the literature. (Ramzan and Bilal [19]) employed a homotopy method (HAM) to obtain power series solutions for three-dimensional flow of viscoelastic conducting nanofluid along a bidirectional stretching sheet with species diffusion and chemical reaction, showing that chemical reaction exerts a strong influence on temperature and nano-particle concentration transfer rate (Sherwood number). They also noted that temperature is elevated whereas nano-particle concentration reduced with increasing Brownian motion parameter whereas primary and secondary velocity are both suppressed with greater viscoelasticity of the nanofluid. (Uddin et al. [20]) studied different order chemical reaction effects on natural convection nanofluid boundary layers using Maple numerical software. They demonstrated that velocities and temperatures are enhanced whereas nanoparticle volume fraction is reduced with increasing order of chemical reaction. Recently, Rashidi et al. [21] studied two dimensional laminar free convective boundary layer flow of an Ostwald-de Waele Power-law nanofluid induced by a steadily rotating infinite disk to a non-darcian fluid past an upward facing chemically reacting horizontal plate saturated in a porous medium by employing OHAM (Optimal Homotopy Analysis Method).

Thermal radiation is traditionally simulated in boundary layer flows with Rosseland's diffusion flux model, which approximates the radiative heat transfer as an algebraic flux model. Several investigators have addressed radiative effects on nanofluid transport. (Turkyilmazoglu and Pop [22]) derived analytical solutions using the Rosseland flux model for radiative heating effects on transient free convection nanofluid boundary layer flows, for copper, titanium, silver, aluminium oxide nanofluids. (Satya Narayana et al. [23]) derived perturbation solutions for radiative magnetic rotating nanofluid flow with heat generation in a porous medium, showing that greater radiative contribution significantly increases nanofluid temperatures. Very recently, (Siva Reddy and Thirupathi [24]) investigated heat and mass transfer effects on natural convection flow in the presence of volume fraction for copper-water nanofluid. (Uddin et al. [25]) investigated radiation flux and hydrodynamic, thermal and solutal slip effects on nanofluid extending/contracting sheet flow with lie group methods and shooting quadrature, noting that heat transfer rates are strongly influenced by radiative heat transfer as are nanoparticle mass transfer rates. Further studies considering thermal radiation in nanofluid convection flows have been reported by (Ibanez et al. [26]) who considered entropy generation in MHD radiative nanofluid slip flow in micro-channels.

The combined influence of Soret and Dufour diffusional phenomena are also a significant area of interest in materials processing systems. Such effects become prominent when species are introduced at a surface in a fluid domain. The relations between the driving potentials and fluxes are of a highly intricate nature. The energy and mass fluxes are generated via composition and temperature gradients respectively. These fluxes are also termed diffusion-thermo (Dufour) and thermal-diffusion (Soret) effects. When both effects occur together, such flows are defined as double-diffusive convection flows. The study of double diffusive natural convection in porous media finds numerous applications in radio-nuclide storage and transport in geological materials, chromatography, bio-chemical contaminant transport in aquifers, filtration technologies, materials fabrication etc. Extensive theoretical and numerical studies of double diffusive convection in both external boundary layer flows and internal flows for different geometrical configurations have been communicated. These include transport from a permeable sphere (El-Kabeir et al. [27]), micropolar convection from a sphere (Beg et al. [28]) heat and mass transfer in inclined square cavities (Chandrasekhar and Kishan, [29]), magnetohydrodynamic flow, heat and mass diffusion from a stretching sheet in porous media (Beg et al. [30]) and boundary layer flow from a conical geometry in porous media, from truncated cone (Rashad and Chamkha [31]). Soret and Dufour effects were shown in these studies to exert a marked influence on velocity, temperature and concentration fields.

The above investigations generally did not consider the collective effects of thermal radiation, viscous dissipation, species and thermal buoyancy or chemical reaction for rotating nanofluid flows. In realistic synthesis operations, these effects are important. Manufacturing of magnetic nanofluids involves frequently high temperature and destructive chemical reaction effects as highlighted by Venkateswarlu and Narayana [37]. Furthermore rotational body force and porous media (filtration media) can be exploited to better control boundary layer processes in such fluids which lead to more homogenous distributions of nanoparticles. Actual flow processes are also unsteady *i.e. time-dependent*, in manufacturing systems as elaborated by Borbath *et al.* [5]. In systems with diffusing species (nano-particles) cross-diffusion effects can also arise. In the present article it is therefore consider transient magnetohydrodynamic (MHD) double-diffusive free convective boundary layer flow of nanofluids from a stationary/moving vertical porous plate in rotating porous media. Wall suction (lateral mass flux) and viscous

heating effects are also incorporated. An attempt is made to investigate comprehensively, the influence of pertinent parameters on primary and secondary velocity distributions for both the stationary plate ($\alpha = 0$) and moving plate ($\alpha = 1$) cases as well as temperature and concentration distributions for three different water-based nanofluids: $Cu - H_2O$ and $Al_2O_3 - H_2O$ and $TiO_2 - H_2O$. Generally two models are popular for simulating nanofluids, namely the (Buongiorno [32]) Buongiorno model (which includes many mechanisms but which emphasizes the contribution of Brownian diffusion and thermophoresis for heat transfer enhancement) and the Tiwari-Das formulation (Tiwari and Das [33]) (which features a nano-particle volume fraction). Very recently, Garoosi et al. [34] used finite volume discretization method to study the natural convection heat transfer of nanofluid in a two-dimensional square cavity containing several pairs of heaters and coolers (HACs) using Buongiorno model. The latter implement in the present study. The transformed boundary layer equations which governs the flow and heat and mass transfer of nanofluids are strongly nonlinear in nature and a numerical method is required for solution of the transformed boundary value problem. The finite element method (FEM) is employed. In section 2 the mathematical model is developed. In section 3 numerical solutions are described with validation and grid-independence. Section 4 contains the discussion and evaluation of the numerical results. Finally the important observations are summarized in the section 5 (Conclusions). The current study is relevant to high-temperature, magnetohydrodynamic (MHD) nanofluid materials processing systems employing rotational body forces.

Mathematical formulation of the problem

The schematic model of the coordinate system and the physical problem under investigation are depicted in Figure 1. The Cartesian coordinate system is selected such that the $x' - axis$ is along the direction of the plate through which fluid flow in the upward direction is considered, $y' - axis$ is perpendicular to the plate and $z' - axis$ is normal to the $x'y' - plane$ i.e. transverse to the plane of the plate. Now consider the magnetohydrodynamic free convection flow with heat and mass transfer (species diffusion) of an electrically-conducting nanofluid from the semi-infinite vertical porous plate adjacent to a homogenous, isotropic porous medium, in the presence of uniform suction in a rotating frame of reference. Darcy's model is employed for porous medium drag effects. The plate is assumed to be in rigid body rotation with constant angular velocity, Ω about the $y' - axis$. A uniform magnetic field of strength, B_0 , is imposed transversely to the flow i.e. along the $y' - axis$.

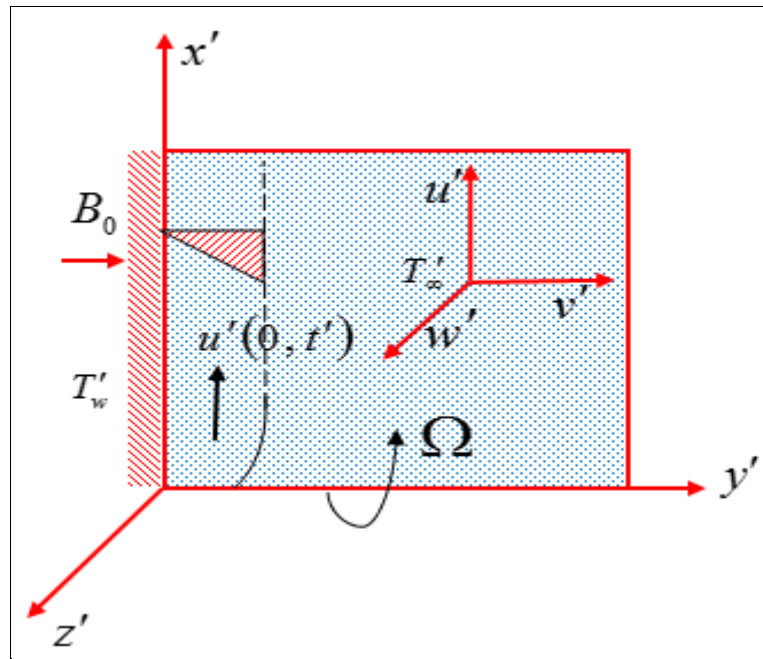


Figure 1. Physical model and coordinate system for the problem.

The plate is moving with the velocity αu_0 , α being a constant. It is assumed that flow is driven by the motion of the plate which oscillates with constant frequency n' in time t' , so that plate temperature oscillates to $T'_w + \varepsilon(T'_w - T'_\infty) \cos n't'$. A uni-directional radiative flux acts normal to the plate surface. The nanofluid which saturates the porous medium is dissipative and is absorbing, emitting and gray but not scattering. Hall current and Maxwell displacement current effects are neglected. Initially at time $t' \leq 0$, both the plate and fluid are maintained at uniform temperature, T'_∞ and uniform nano-particle concentration C'_∞ . Once the plate starts moving *i.e.*, when $t' > 0$ along x' -axis direction against gravitational field, the temperature is raised to T'_w which is higher than the ambient temperature T'_∞ and the species (nano-particle) concentration at the surface is maintained uniformly at C'_w . Since the plate is assumed to be of infinite extent along x' and y' directions then all the physical quantities are dependent solely on t' and y' . In comparison with the external magnetic field applied, it is assumed that induced magnetic field is negligible since the magnetic Reynolds number of flow is taken to be very small (Liron and Wilhelm [35]). Thus this assumption is justified, since the magnetic Reynolds number is very small for metallic liquids and partially ionized fluids. Finally, it is also assumed that there is no applied voltage then there is no external electric field is applied so that the polarization of the fluid is negligible (Cramer and Pai [36]), the base fluid and suspended nano particles are in thermal equilibrium state, the nanoparticles are assumed to have a uniform shape, size and plate is electrically non-conducting and the reaction is assumed to take place entirely in the stream.

By considering the aforementioned assumptions the governing boundary layer equations of conservation of mass, momentum, energy and concentration equations by following Venkateswarlu and Satya Narayana [37] for unsteady free convective flow under the Boussinesq approximation are given by:

$$\frac{\partial w'}{\partial y'} = 0 \quad (1)$$

$$\begin{aligned} \rho_{nf} \left(\frac{\partial u'}{\partial t'} + w' \frac{\partial u'}{\partial y'} - 2\Omega v' \right) &= \mu_{nf} \frac{\partial^2 u'}{\partial y'^2} + g(\rho\beta)_{nf} (T' - T'_\infty) + g(\rho\beta)_{nf} (C' - C'_\infty) \\ &\quad - \sigma_{nf} B_0^2 u' - \frac{v_f u'}{k} \end{aligned} \quad (2)$$

$$\rho_{nf} \left(\frac{\partial v'}{\partial t'} + w' \frac{\partial v'}{\partial y'} + 2\Omega u' \right) = \mu_{nf} \frac{\partial^2 v'}{\partial y'^2} - \sigma_{nf} B_0^2 v' - \frac{v_f v'}{k} \quad (3)$$

$$(\rho c_p)_{nf} \left(\frac{\partial T'}{\partial t'} + w' \frac{\partial T'}{\partial y'} \right) = k_{nf} \frac{\partial^2 T'}{\partial y'^2} - \frac{\partial q_r}{\partial y'} + \mu_{nf} \left(\frac{\partial u'}{\partial y'} \right)^2 + \frac{D_m k_t}{c_s c_p} \frac{\partial^2 C'}{\partial y'^2} \quad (4)$$

$$\left(\frac{\partial C'}{\partial t'} + w' \frac{\partial C'}{\partial y'} \right) = D_m \frac{\partial^2 C'}{\partial y'^2} - k_r (C' - C'_\infty) + \frac{D_m k_t}{T'_m} \frac{\partial^2 T'}{\partial y'^2} \quad (5)$$

The final terms on the right hand side of equations (2) and (3) represent the Darcian linear drag forces for the primary and secondary flow respectively. The corresponding initial and boundary conditions (Ishigaki [38]; Ganapathy [39]; Das et al. [40]) on the vertical surface and in the freestream can be defined as:

$$\left. \begin{aligned} \text{for } t' \leq 0 \quad \{ \forall y' \quad & u'(y', t') = 0, \quad v'(y', t') = 0, \quad T' = T'_\infty, C' = C'_\infty \\ \text{for } t' > 0 \quad \left\{ \begin{array}{l} y' = 0 \quad u'(0, t') = \alpha u_0, \quad v'(0, t') = 0, \\ T'(0, t') = T'_w + \varepsilon (T'_w - T'_\infty) \cos n't', \quad C' = C'_w \\ y' \rightarrow \infty \quad u'(\infty, t') \rightarrow 0, \quad v'(\infty, t') \rightarrow 0, \quad T'(\infty, t') \rightarrow T'_\infty, C'(\infty, t') \rightarrow C'_\infty \end{array} \right. \end{aligned} \right\} \quad (6)$$

Here u' , v' are velocity components along x' and z' directions respectively and α denotes the direction of motion of the plate. When $\alpha = 0$ the plate is said to be in stationary state and when $\alpha = 1$ this corresponds to the case where the plate is moving vertically upwards. It is worth mentioning here that nomenclature is presented in Appendix 1. The nanofluid properties (Oztop and Abu-Nada [41]) are given by:

$$\left. \begin{aligned} \rho_{nf} &= (1-\phi)\rho_f + \phi\rho_s, \quad (\rho c_p)_{nf} = (1-\phi)(\rho c_p)_f + \phi(\rho c_p)_s \\ \sigma_{nf} &= \sigma_f \left[1 + \frac{3(\sigma-1)\phi}{(\sigma+2) - (\sigma-1)\phi} \right], \quad (\rho\beta)_{nf} = (1-\phi)(\rho\beta)_f + \phi(\rho\beta)_s, \quad \sigma = \frac{\sigma_s}{\sigma_f} \end{aligned} \right\} \quad (7a)$$

The effective thermal conductivity of the nanofluid is adopted from Brinkman [42] model as

$$\mu_{nf} = \frac{\mu_f}{(1-\phi)^{2.5}} \quad (7b)$$

The effective thermal conductivity of the nanofluid is given by Maxwell-Garnets model followed by Oztop and Abu-Nada [41]

$$K_{nf} = K_f \left[\frac{K_s + 2K_f - 2\phi(K_f - K_s)}{K_s + 2K_f + 2\phi(K_f - K_s)} \right] \quad (7c)$$

The continuity equation $\nabla \cdot \vec{q} = 0$ leads to the reduced mass conservation equation $\frac{\partial w'}{\partial y'} = 0$. On integrating this results $w' = -w_0$, where constant w_0 is the normal suction velocity at the plate

and \bar{q} is constant. For an optically thick (photon mean free path is very small) fluid, in addition to emission there is also self-absorption and usually the absorption coefficient is wavelength dependent so thus the net radiative heat flux term (Brewster [43]) is then approximated using the Rosseland diffusion model as:

$$q_r = \frac{-4\sigma^*}{3k^*} \frac{\partial T'^4}{\partial y'} \quad (8)$$

Here k^* and σ^* are the Rosseland mean absorption coefficient and Stefan-Boltzmann constant ($5.6697 \times 10^{-8} \text{Wm}^{-2}\text{K}^{-4}$) respectively. This model has been applied in a diverse range of both magnetic and non-magnetic heat and mass transfer problems and has been shown to be quite accurate for optically-dense regimes, as elaborated by (Beg et al. [44-47]). It is assumed that the temperature difference within the flow are sufficiently small such that T'^4 may be expressed as a linear function of the temperature by expanding in a Taylor series about T'_∞ as $T'^4 \cong T'_\infty^4 + 4T'_\infty^3(T' - T'_\infty) + 6T'_\infty^2(T' - T'_\infty)^2 + \dots$, and by neglecting the higher order terms it gives:

$$T'^4 \cong 4T'_\infty^3 T' - 3T'_\infty^4 \quad (9)$$

Hence, from Eq. (8), using Eq. (9), the resultant is:

$$\frac{\partial q_r}{\partial y'} = -\frac{16\sigma^* T'_\infty^3}{3k^*} \frac{\partial^2 T'}{\partial y'^2} \quad (10)$$

Proceeding with the analysis, a set of *non-dimensional* variables defined as follows:

$$\left. \begin{aligned} y &= \frac{u_o y'}{v_f}, u = \frac{u'}{u_o}, v = \frac{v'}{u_o}, t = \frac{u_o^2 t'}{v_f}, n = \frac{v n'}{u_o^2}, S = \frac{w_o}{u_o}, K = \frac{\rho_f k u_o^2}{v_f^2}, Kr = \frac{k_r v_f}{u_o^2}, k^2 = \frac{\Omega v_f}{u_o^2}, Sc = \frac{v_f}{D_m}, \\ \theta &= \frac{T' - T'_\infty}{T'_w - T'_\infty}, C = \frac{C' - C'_\infty}{C'_w - C'_\infty}, M^2 = \frac{\sigma_f B_o^2 v_f}{\rho_f u_o^2}, R = \frac{16\sigma^* T'_\infty^3}{3k k^*}, Pr = \frac{(\rho c_p)_f v_f}{k_f}, Ec = \frac{u_o^2}{(\rho c_p)_f (T'_w - T'_\infty)}, \\ Gr &= \frac{g \beta_f v_f (T'_w - T'_\infty)}{u_o^3}, Gc = \frac{g \beta_f v_f (C'_w - C'_\infty)}{u_o^3}, Sr = \frac{D_m K t (T'_w - T'_\infty)}{T'_m v_f (C'_w - C'_\infty)}, Du = \frac{D_m K t (C'_w - C'_\infty)}{c_s c_p v_f (T'_w - T'_\infty)} \end{aligned} \right\} \quad (11)$$

Substituting nanofluid properties and the above dimensionless variables i.e., equations (7a)-(7c), (10) and (11) into equations (2) – (4) yields the following system of unsteady coupled, non-dimensional nonlinear partial differential equations.

$$\frac{\partial u}{\partial t} - S \frac{\partial u}{\partial y} - 2k^2 v = A_1 \frac{\partial^2 u}{\partial y^2} - Gr A_2 \theta + Gc A_2 C - A_3 \left(M^2 + \frac{1}{K} \right) u \quad (12)$$

$$\frac{\partial v}{\partial t} - S \frac{\partial v}{\partial y} + 2k^2 u = A_1 \frac{\partial^2 v}{\partial y^2} - A_3 \left(M^2 + \frac{1}{K} \right) v \quad (13)$$

$$\frac{\partial \theta}{\partial t} - S \frac{\partial \theta}{\partial y} = A_4 \frac{\partial^2 \theta}{\partial y^2} + Ec \left(\frac{\partial u}{\partial y} \right)^2 + Du \left(\frac{\partial^2 C}{\partial y^2} \right) \quad (14)$$

$$\frac{\partial C}{\partial t} - S \frac{\partial C}{\partial y} = \frac{1}{Sc} \frac{\partial^2 C}{\partial y^2} - Kr C + Sr \left(\frac{\partial^2 \theta}{\partial y^2} \right) \quad (15)$$

Where $A_1 = \frac{1}{(1-\phi)^{2.5} \rho_{nf}}$, $A_2 = \frac{(\rho c_p)_{nf}}{(\rho\beta)_{nf}}$, $A_3 = \frac{\sigma_{nf}}{\rho_{nf}}$, $A_4 = \frac{1}{(\rho c_p)_{nf} \text{Pr}} (K_{nf} + R)$.

These expressions contain nano-particle volume fraction and other property contributions. The appropriate initial and boundary conditions in non-dimensional form take the form:

$$\left. \begin{array}{l} \text{for } t \leq 0 \quad \{ \forall y \quad u(y,t) = 0, \quad v(y,t) = 0, \quad \theta(y,t) = 0, \quad C(y,t) = 0 \\ \text{for } t > 0 \quad \left\{ \begin{array}{l} \text{at } y = 0 \quad u(0,t) = \alpha, \quad v(0,t) = 0, \quad \theta(0,t) = 1 + \varepsilon \cos nt, \quad C(0,t) = 1 \\ \text{as } y \rightarrow \infty \quad u(\infty,t) \rightarrow 0, \quad v(\infty,t) \rightarrow 0, \quad \theta(\infty,t) \rightarrow 0, \quad C(\infty,t) \rightarrow 0 \end{array} \right. \end{array} \right\} \quad (16)$$

Finite element computational solutions and validation

The transformed system of non-linear, coupled and non-homogeneous dimensionless partial differential equations (12) - (15) under the boundary conditions equation (16) are solved numerically by using the extensively-validated and robust finite element method with a Galerkin weighted residual scheme. This method comprises five fundamental steps, namely discretization of the domain, derivation of the element equations, assembly of element equations, imposition of boundary conditions and finally iterative solution of the assembled equations with a robust method e.g. Cholesky decomposition, Gaussian elimination etc. Details of the finite element approximations are provided in the Appendix 2. An excellent description of these steps are presented in the text books of (Reddy [48]) and Further details of this methodology as applied to nanofluids are given in (Rana et al. [49]). Dimensionless primary velocity (u), secondary velocity (v), temperature (θ) and nano-particle concentration (C) are computed.

The grid independence is conducted by dividing the entire domain into successively sized grids of mesh density $131 \times 131, 151 \times 151$ and 171×171 . The boundary conditions for y at ∞ are replaced by a sufficiently large value where the velocity, temperature and concentration profiles approach zero. The MAPLE-based FEM code is ran when the suction parameter $S = 0.5$ for different step sizes and very good agreement between the results for all the profiles is achieved as presented in Table 1. After many trials for computational flexibility $y_{\max} = 8$ is imposed where $y_{\max} \rightarrow \infty$ i.e., external to the momentum, energy and concentration boundary layers and here adopted for all the computations, 150 intervals of equal step size 0.053. At each node, four functions are to be evaluated, so that following assembly of elements a set of 604 non-linear equations are formed. Therefore an iterative scheme is adopted and by introducing boundary conditions the system of equations are solved systematically. The solution is assumed to be converged when the solution difference satisfies the desired accuracy 10^{-7} . An excellent convergence for all the results is achieved. Thermo-physical properties of H_2O , Cu , Ag , Al_2O_3 and TiO_2 -water nanofluids are adopted from (Oztop and Abu-Nada [41]) and documented in Table 2. Furthermore, it is important to calculate the engineering quantities of interest. These include the *skin-friction* (surface wall shear stress function) which is obtained as $C_f = \mu_{nf} \left(\frac{\partial u}{\partial y} \right)_{y=0}$. The rate of the heat transfer at the plate is defined as a *Nusselt number*

and given by $Nu = -K_{nf} \left(\frac{\partial \theta}{\partial y} \right)_{y=0}$. The rate of mass transfer of nano-particles at the wall is

computed using the *Sherwood number* which is given by $Sh = -\mu_{nf} \left(\frac{\partial C}{\partial y} \right)_{y=0}$.

In order to validate the accuracy of the numerical results obtained through the MAPLE-based finite element code, the present results are compared for skin friction and Nusselt number with the results obtained through earlier analytical studies. The current model reduces to that of (Hamad and Pop [18]) in the absence of thermal radiation, heat generation and mass transfer (i.e. neglecting the species diffusion equation and associated terms). The comparison is documented in Table 3, showing very good correlation. Furthermore comparisons of the present finite element solutions with (Venkateswarlu and Satya Narayana [37]) have also been conducted, for the case of constant surface temperature and oscillatory plate velocity without heat generation terms and these are shown in Table 4. The comparisons confirms that the present results are indeed valid and in agreement with the published literature. Therefore, these favorable comparisons justify confidence in the finite element code employed which can be used therefore in presenting further results quantitatively and graphically.

Results and discussion

Extensive numerical computations have been performed with the finite element code. Here this article address the influence of k^2 , M^2 , Sr , Du , Gr , Gc , Ec , ϕ , R , Pr , Sc and Kr on the nanofluid velocity, temperature and species concentration distributions. Solutions are depicted graphically in Figures 2 to 26. Numerical solutions are illustrated in these figures by fixing the values $n = 10$, $nt = \pi/2$, $\varepsilon = 0.02$, $t = 0.19$ and $K = 0.5$ (time is therefore not explicitly studied in the Figures 2 to 26). The CPU took 1.31 seconds for 151 nodal points with the Intel core i3 processor under windows platform, which is computed by using the Maple command `time ()` for computation of velocity, temperature and concentration profiles. The following default values were adopted to represent physically realistic flows for finite element computation as follows: $k^2 = 4$, $S = 1.0$, $M^2 = 1.0$, $Sr = 1.3$, $Du = 0.15$, $Gr = 5$, $Gc = 4$, $Ec = 0.001$, $\phi = 0.1$, $R = 0.5$, $Pr = 6.2$, $Sc = 0.45$ and $Kr = 0.5$. It is noted that the influence of some parameters on physical quantities are not presented graphically for brevity and are noted in other studies of nanofluid boundary layers. A parametric investigation is now undertaken to elucidate the thermo-physical characteristics of the flow. In all plots the asymptotic profiles for large y confirm that an adequately large boundary condition is imposed in the freestream and that solutions are indeed correctly converged.

Figures 2 to 5 depict the primary (u) and secondary (v) velocity (for $\alpha = 0$ and $\alpha = 1$ cases), temperature and concentration profile distributions for three different water-based nanofluids $Cu - H_2O$ (copper water), $Al_2O_3 - H_2O$ (Aluminium oxide-water) and $TiO_2 - H_2O$ (Titanium oxide-water). Figure 2 demonstrates that both primary and secondary velocity profiles for the stationary plate scenario ($\alpha = 0$) are initially zero (the plate is stagnant) and with progressive distance along the plate in the y -direction, values grow as the boundary layer grows. The peak magnitudes in both cases are attained relatively close to the leading edge and thereafter decreased to zero at a sufficiently large value of y . Thus, substantially larger magnitudes of both primary and secondary velocity are observed for $Cu - H_2O$ nanofluid. Progressively

lower values correspond to the $Al_2O_3 - H_2O$ and $TiO_2 - H_2O$ nanofluids. Significant flow acceleration is therefore achieved with $Cu - H_2O$ nanofluid whereas strong deceleration is associated with the $Al_2O_3 - H_2O$ and $TiO_2 - H_2O$ nanofluids. Figure 3 shows that a very different response in the primary and secondary velocity profiles is computed for the moving plate ($\alpha = 1$) scenario. For this case, primary velocity commences with the actual moving plate velocity and progressively decreases to zero asymptotically in the freestream. Primary velocity exhibits monotonic decay for all nanofluid types. However secondary velocity reveals a similar pattern as observed in the stationary plate case, in that magnitude of the secondary velocity profiles grows from the leading edge, peaks some distance from the leading edge and then decays asymptotically to zero, in accordance with the freestream boundary conditions. Generally significantly greater magnitudes of secondary velocity are sustained compared with primary velocity with distance along the plate (y). Higher values of primary velocity are computed for the stationary plate at intermediate distances from the leading edge, whereas for the moving plate scenario the value at the wall is maximized. It is also interesting to note that a slight displacement in peak secondary velocity occurs when the nanofluid is changed from $Cu - H_2O$ to $Al_2O_3 - H_2O$ and then to $TiO_2 - H_2O$. As with the stationary plate scenario, Titanium oxide-water nanofluid attains lowest primary and secondary velocity magnitudes whereas the copper-water nanofluid consistently attains highest magnitudes. Figures 4 and 5 demonstrate that temperature (θ) and concentration (C) profiles for $Cu - H_2O$ are markedly higher as compared with the $Al_2O_3 - H_2O$ and $TiO_2 - H_2O$ nanofluids. This is attributable to the high thermal conductivity of Cu relative to Al_2O_3 and TiO_2 which manifests in an enhancement of the thermal and species diffusion in the boundary layer regime. As a result the thermal and concentration boundary layer thicknesses for $Cu - H_2O$ nanofluid are greater than for Al_2O_3 and TiO_2 nanofluids. The profiles for temperature and concentration are always monotonic decays from the leading edge to the freestream. A greater modification in magnitudes is achieved for temperatures compared with concentrations.

Figures 6 and 7 present the response in primary and secondary (cross flow) velocity profiles again for both cases of a stationary and a moving plate, for different values of rotational parameter (k^2) and the three different nanofluid suspensions. The rotational parameter features in the Coriolis body force terms arising in both the dimensionless primary momentum equation (12) and the dimensionless secondary momentum equation (13). These terms are respectively $-2k^2v$ and $+2k^2u$, respectively. The term $k^2u = \Omega v_f / u_0^2$ is directly proportional to the angular velocity of the rotating plate. As k^2 is increased the Coriolis force is also enhanced i.e. the rotation of the plate is more intense but the body force which is negative for primary flow becomes stronger also and this leads to a significant deceleration in the primary and secondary flow (note the plate is stationary only in the sense that it is not moving vertically upwards for $\alpha = 0$ in Figure 6). Although the secondary rotational body force is increased, the dominant effect is that of the primary rotational body force (Coriolis force) which leads to a concurrent deceleration also in the secondary flow i.e. damping of the flow velocity. These observations are also consistent with classical Newtonian rotating plate flow studies documented in (Greenspan [48]). The trends computed in Figure 6 are also in general agreement with the findings of Venkateswarlu and Satya Narayana [37] for rotating plate nanofluid dynamics. In Figure 6 it is observed that the primary and secondary velocity magnitudes are considerably greater for $Cu - H_2O$ nanofluid compared with $Al_2O_3 - H_2O$

nanofluid. Although retardation of the flow is prominent, flow reversal is never observed i.e. magnitudes of both primary and secondary velocity remain positive for all values of y irrespective of the magnitude of k^2 or the nanofluid case. In Figure 7, for the vertically upward moving plate scenario ($\alpha = 1$), again the primary and secondary velocity profiles are markedly different. There is a gradual decay in primary velocity from the leading edge with distance y to vanishing velocity in the freestream. However the secondary velocity profile is similar to the case in Figure 6 for the stationary plate scenario with zero magnitude at the leading edge, followed by a peak shortly thereafter and then a progressive decay to the freestream. Both velocity components however decrease (as in Figure 6) with greater values of the rotational parameter and again highest magnitudes correspond to the $Cu - H_2O$ nanofluid whereas lowest magnitudes are associate with $Al_2O_3 - H_2O$ nanofluid.

Figures 8 and 9 depict the primary and second velocity profile response to a change in magnetic field parameter (M^2). The primary and secondary momentum equations i.e. Eqs. (12) and (13) each feature a Lorentzian magnetohydrodynamic body force component, specifically $-M^2u$ and $-M^2v$. Both primary and secondary velocity fields are therefore directly influenced by the magnetic field effect. The parameter M is related directly to the applied magnetic field strength, B_0 . Increasing magnetic field strength therefore elevates the Lorentzian drag force which inhibits both primary and secondary flows, for both stationary and moving plate cases. Effectively the application of transverse magnetic field to the electrically-conducting nanofluid generates a resistive type force, which acts against the motion of the nanofluid. When $M^2 = 1$ the magnetic body force is equal to the viscous hydrodynamic force. For $M^2 > 1$ the magnetic force is dominant. The deceleration (retardation) in the boundary layer flow results in an increase in momentum boundary layer thickness. For the stationary plate case (Figure 8), peak velocity arises some distance from the leading edge and as noted in earlier graphs, decays asymptotically to zero at the edge of hydrodynamic boundary layer. For the moving plate scenario (Figure 9) again primary velocity is a maximum at the leading edge and drops gradually to vanish in the freestream, whereas the secondary velocity assumes a similar behavior to the stationary plate scenario and again peaks close to the leading edge i.e. exhibits a parabolic profile. For both plate cases, $Cu - H_2O$ nanofluid achieves greater acceleration than $Al_2O_3 - H_2O$ nanofluid. Again it is apparent that despite the strong magnetic field values considered, flow reversal (backflow) is never induced in either the primary or secondary flows. However the application of a magnetic field achieves excellent flow control in the regime and provides a simple but effective mechanism for regulating nanomaterial's processing operations.

Figures 10 to 13 display influence of thermo-diffusive Soret number (Sr) and diffuso-thermo Dufour number (Du) on the primary and secondary velocity for both the cases of stationary and moving plates. Soret number arises in the term, $+Sr\left(\frac{\partial^2\theta}{\partial y^2}\right)$ in the concentration conservation equation (15). This term represents the influence of temperature gradient on the concentration field. It is therefore one of two cross-diffusion terms, the other being, $+Du\left(\frac{\partial^2 C}{\partial y^2}\right)$ which arises in the temperature equation (14), features the Dufour number and signifies the influence of concentration gradient on the temperature field. In Figures 10 and 11,

an increase in Soret number (Sr) is found to generally enhance the primary and secondary velocity magnitudes for all values of the coordinate y . The magnitudes of primary velocity are however significantly greater for the stationary plate case (Figure 10). For the moving plate case (Figure 11) again higher values of primary velocity arise at the leading edge but elsewhere the secondary velocity is found to be greater. Increasing Soret number therefore evidently aids in momentum development and accelerates both primary and secondary flow component velocities. Again copper-water nanofluid achieves consistently greater magnitudes of both primary and secondary velocity compared with aluminium oxide nanofluid. Figures 12 and 13 show that increasing Dufour number exerts a similar influence to Soret number i.e. it enhances both primary and secondary velocities. Overall therefore the contribution of both cross diffusion gradients is assistive to the primary and secondary flow fields.

Figures 14 and 15 present the response in primary (u) and secondary (v) velocity to various thermal Grashof numbers (Gr). Thermal Grashof numbers signifies the relative magnitude of the thermal buoyancy force and the opposing frictional force (viscous hydrodynamic force) acting on the water-based nanofluids. Physically $Gr > 0$, $Gr < 0$, $Gr = 0$ represent cooling of the plate, heating of the plate and absence of free convection currents respectively (this last case corresponds to forced thermal convection where $Gr = 0.0$ eliminates the thermal buoyancy force term, $GrA2C$ in the primary momentum equation (12)). The thermal buoyancy term therefore couples the primary momentum equation (12) with the energy conservation equation (14). Since the non-zero values specified for Gr are 5 or -5, the thermal buoyancy force dominates over the viscous force (only when $Gr = \pm 1$ are both forces of equivalent magnitude). For the stationary plate case (Figure 14), negative Grashof number clearly induces a deceleration in the primary flow whereas positive Grashof number accelerates the flow. Assistive thermal buoyancy (cooling of the plate) therefore aids in momentum development whereas opposing thermal buoyancy (heating of the plate) destroys momentum. The converse effect is computed for the secondary flow field however where cooling of the plate ($Gr = 5.0$) is observed to accelerate the flow (less negative values of secondary velocity) whereas heating of the plate ($Gr = -5.0$) induces strong deceleration (greater negative values of secondary velocity). The secondary flow for the stationary plate case is always reversed since values of v are always negative. Only positive values of primary velocity are computed indicating that backflow does not arise in the primary flow field. It is evident from Figure 14 that the shape of the primary velocity and magnitude of the secondary velocity for the case of stationary plate are the same but in opposite directions i.e. the primary and secondary velocity components demonstrate a symmetry about the line $y = 0$. Thermal buoyancy however does not feature in the secondary momentum equation (13) implying that the impact on secondary velocity is indirectly experienced via coupling with the primary momentum equation (12). Generally $Cu - H_2O$ nanofluid induces strong acceleration in both the primary and secondary flow compared with $Al_2O_3 - H_2O$ nanofluid. Profiles for both primary and secondary flow for the moving plate scenario (Figure 15) deviate significantly from the stationary plate scenario (Figure 14). In both flow fields, reversal of flow is never observed. Primary velocity decays, as noted in earlier plots from a maximum at the leading edge to a minimum in the freestream, whereas secondary velocity ascends from zero at the leading edge to peak a short distance from this point and then decays smoothly to zero. Again $Cu - H_2O$ nanofluid results in much greater primary and secondary velocity values than $Al_2O_3 - H_2O$ nanofluid. The moving plate scenario also achieves generally a more stable flow pattern for both primary and secondary components since backflow is completely eliminated in this case.

Figures 16 and 17 depict the evolution in primary and secondary flow velocities for both cases of stationary and moving plates, respectively, with variation in solutal Grashof number (Gc). The solutal (nano-particle species) buoyancy force also arises solely in the primary momentum equation (13) via the term $GcA2C$. This term effectively couples the primary momentum equation (12) directly to the nano-particle species (concentration) conservation equation (14). Only values of $Gc > 0$ are considered i.e. 2, 2.2 and 2.4 for which the species buoyancy force significantly exceeds the viscous force in the regime. Reverse flow is never computed in either Figure 16 and 17 since only assistive species buoyancy forces are present ($Gc > 0$). In Figure 16 (stationary plate flow case) the primary velocity and secondary velocity are both enhanced with greater (Gc) values and $Cu - H_2O$ nanofluid achieves markedly greater magnitudes than the $Al_2O_3 - H_2O$ nanofluid. In Figure 1 (moving plate scenario), the customary response in primary and secondary velocity distributions is observed. Primary velocity peaks at $y = 0$ and descends to vanish for large y . Secondary velocity climbs from zero at $y = 0$ and thereafter exhibits a parabolic profile with increasing y values. Increasing species Grashof number, (Gc) clearly induces a strong acceleration in both the primary and secondary flow. As before the magnitudes are lower however for $Al_2O_3 - H_2O$ nanofluid compared with $Cu - H_2O$ nanofluid, a characteristic again probably caused by the greater thermal conductivity of the copper nano-particles. Figures 14 to 17 strongly emphasize that both thermal and species buoyancy exert a non-trivial influence on velocity components in the nanofluid boundary layer flow regime.

Figures 18 and 19 illustrate the modification in primary (u) and secondary (v) velocity components for the stationary and moving plate cases, with different values of the nano-particle volume fraction (ϕ). As volume fraction increases, the thermal conductivity of nanofluid is elevated. Therefore thermal diffusion is assisted in the regime. Primary and secondary velocity magnitudes are however strongly decreased with increasing (ϕ) values as seen in Figure 18 for the stationary plate case. Although primary velocity is greater initially than secondary velocity, with progressive distance along the plate i.e. greater y values, this trend is reversed and secondary velocity weakly exceeds primary velocity far from the leading edge i.e. closer to the freestream. Here $Cu - H_2O$ nanofluid again achieves consistently greater magnitudes of both primary and secondary velocity as compared with $Al_2O_3 - H_2O$ nanofluid. However, further note that the primary velocity magnitudes even with $Al_2O_3 - H_2O$ nanofluid are distinctly greater than the secondary velocity values with $Cu - H_2O$ nanofluid. Figure 19 shows that for the moving plate case, a significant deceleration is also computed in both primary and secondary velocity components with greater nanoparticle volume fraction (ϕ). The influence on primary velocity is consistent however for all values of the coordinate along the plate (y) whereas it is only sustained for a finite distance for the secondary velocity and the reverse effect is observed near the freestream (as in Figure 18). Significantly lower magnitudes of the primary velocity are computed in Figure 19 as compared with Figure 18. However the dominance of $Cu - H_2O$ nanofluid over $Al_2O_3 - H_2O$ nanofluid is maintained even in the moving plate scenario i.e. copper water nanofluid achieves better performance.

Figure 20 illustrates the effect of Rosseland thermal radiation parameter, R on temperature distributions for $Cu - H_2O$ and $Al_2O_3 - H_2O$ nanofluids. It is evident that with greater R

values temperatures are markedly enhanced throughout the boundary layer along the plate. Thermal radiation arises in the augmented thermal diffusion term in the energy conservation equation (14) i.e. $A_4 \frac{\partial^2 \theta}{\partial y^2}$ where $A_4 = \frac{1}{(\rho c_p)_{nf} Pr} (K_{nf} + R)$ and $R = \frac{16\sigma^* T_\infty^3}{3kk^*}$ relates the relative role of thermal radiative heat transfer to thermal conduction heat transfer. When $R = 1$ both modes contribute equally. When $R < 1$ thermal conduction dominates and when $R > 1$ thermal radiation dominates. For the values of R examined in Figure 20 i.e. 0.1, 0.2, 0.3, 0.4 the contribution of thermal radiation is progressively greater. This intensifies the heat transfer and energizes the nanofluid boundary layer which manifests in an elevation in temperatures. Copper water nanofluid again responds more successfully than aluminium oxide water nanofluid to a change in radiative flux since it consistently attains higher temperatures. The effect of thermal radiation is therefore very significant on the variation of temperature. It is seemed that temperature increases rapidly in an increase in the thickness of thermal boundary layer. Nanofluid material properties may therefore be strongly manipulated via the imposition of a relatively weak radiative flux in manufacturing operations.

Figure 21 depicts the influence of Dufour number on temperature distributions. The contribution of concentration gradients to thermal energy flux in the flow regime is measured with the Dufour number (Du). From the graph it is noticed that temperature increases strongly with an increase in Dufour number (Du) and this results in an elevation in thermal boundary layer thickness. This is due to increase in convective heat exchange at the plate surface. The cross diffusion term, $+ Du \left(\frac{\partial^2 C}{\partial y^2} \right)$ which arises in the temperature equation (14), therefore exerts a prominent effect on temperatures in the boundary layer. Again it is noted that $Cu - H_2O$ attains substantially greater temperatures for all values of the y -coordinate as compared with $Al_2O_3 - H_2O$ nanofluid.

Figure 22 presents the variations in the temperature profiles for different values of Prandtl number (Pr). Prandtl number refers to the relative contribution of momentum diffusion to thermal diffusion in the boundary layer regime. Furthermore, an increase of Prandtl number results in a decrease in temperature distribution in thermal boundary layer. The physical reason is that smaller values of Prandtl number are associated with greater thermal conductivity, and therefore heat is able to diffuse away from the heated surface more rapidly than at higher values of Prandtl number i.e. the energy diffusion rate is greater than the momentum diffusion rate for $Pr < 1$ whereas the converse is evident for $Pr > 1$. For $Pr = 1$ both the energy and momentum diffusion rates are equivalent and the momentum and thermal boundary layer thicknesses the same. Effectively the rate of heat transfer is reduced and an increase in Pr induces a reduction in thickness of the thermal boundary layer. Significantly greater temperatures are however computed with copper water nanofluid relative to aluminium oxide water nanofluid at any Prandtl number, indicating that thermal conductivity of nano-particles has a dominant influence in nanofluid boundary layer transport phenomena.

Figure 23 presents the evolution in temperature profiles with variation in Eckert number (Ec). This parameter is associated with the viscous heating effect and is usually very small for incompressible flows, as studied here and further elaborated in (Gebhart et al. [50]). It expresses the relationship between the kinetic energy in the flow and the boundary layer

enthalpy difference. It therefore represents the quantity of conversion of kinetic energy into internal energy by work done against the viscous fluid stresses. An increase in Eckert number via dissipation of mechanical energy (caused by internal friction between molecules of the nanofluid) into thermal energy (heat) will enhance the temperature of the water-based nanofluids in the porous regime, as observed in Figure 23. The classical velocity overshoot observed in many studies is also computed in Figure 23, and arises near the plate leading edge. Smooth decay of temperatures following this peak are computed into the freestream. Thermal boundary layer thickness is generally enhanced with greater Eckert number and again the effect is more prominent in copper water nanofluids than in aluminium oxide water nanofluids.

Figures 24 to 26 represent the influence of Schmidt number (Sc), Soret number (Sr) and chemical reaction parameter (Kr) on nano-particle concentration profiles respectively. Figure 24 reveals that there is a sustained reduction in concentration magnitudes of nano-particle species with increasing Schmidt number. The Schmidt number represents the ratio of the momentum diffusivity to the mass (nano-particle species) diffusivity, i.e. it relates the thickness of the hydrodynamic boundary layer to that of the concentration boundary layer. It also relates the momentum (viscous) diffusion rate to the molecular (nano-particle) diffusion rate. For $Sc < 1$ momentum diffusion is dominated by molecular diffusion. For $Sc = 1$ both diffusion rates are the same. For $Sc > 1$ momentum diffusion rate exceeds molecular diffusion rate. As Sc is increased the nano-particle molecular diffusivity is reduced. This results in decreasing species diffusion rates and a lowering in nano-particle concentration magnitudes throughout the boundary layer. Physically this also manifests in a decrease in the nano-particle concentration boundary layer thickness with increasing Schmidt number. Irrespective however of the Schmidt number, the copper-water nanofluid again achieves higher concentration values than the aluminium oxide water nanofluid. In Figure 25, it is observed that an increase in Soret number (Sr) induces a significant enhancement in concentration profiles which in turn increase the thickness of species concentration boundary layer. Near the plate surface species concentration strongly exceeds that in the freestream. The term, $+Sr\left(\frac{\partial^2\theta}{\partial y^2}\right)$ in the concentration conservation equation (15), therefore boosts concentration magnitudes strongly. Hence temperature gradients exert a significant influence on the nano-particle species diffusion in the boundary layer. Greater concentration boundary layer thickness is achieved with copper-water nanofluid compared with aluminium oxide water nanofluid. Finally Figure 26 shows that with increasing chemical reaction parameter ($Kr > 0$) magnitudes of concentration are markedly reduced. The term $-KrC$ in equation (15) indicates a destructive chemical reaction in which nano-particle species is decreased in the regime for $Kr > 0$. This results in depletion also in nano-particle concentration boundary layer thickness. In both Figures 25 and 26 it is observed again that $Cu - H_2O$ nanofluid invariably attains much greater nano-particle concentration magnitudes for all values of the y-coordinate as compared with $Al_2O_3 - H_2O$ nanofluid. Higher concentration boundary layer thickness will therefore also be associated with $Cu - H_2O$ nanofluid.

Conclusions

A mathematical model has been presented for the transient incompressible MHD double diffusive free convective boundary layer flow of nanofluids from a rotating vertical porous plate considering buoyancy, thermal radiation, viscous heating and chemical reaction effects. The non-dimensionalized partial differential equations for primary and secondary momentum, energy and species conservation which govern the flow problem have been solved numerically by using robust finite element method. Validation of solutions with earlier published results has been included. Mesh-independence study has also been conducted. Both cases of an upwardly moving plate and a stationary plate have been considered. Results have been computed and depicted graphically for influence of k^2 , M^2 , Sr , Du , Gr , Gc , Ec , ϕ , R , Pr , Sc and Kr on the nanofluid velocity, temperature and species concentration distributions. Furthermore a variety of water based nanofluids i.e. $Cu - H_2O$, $Al_2O_3 - H_2O$ and $TiO_2 - H_2O$ nanofluids have been considered. The numerical solutions have been presented at a selected time interval. The principal findings of the current investigation are summarized below.

- The primary and secondary flow are both accelerated with increasing values of Sr, Du, Gr and Gc , while they are decelerated with increasing values of k^2, M^2 and ϕ for both stationary and moving plate cases. $Cu - H_2O$ nanofluid velocity distributions attains zero velocity asymptotically faster than the $Al_2O_3 - H_2O$ nanofluid
- An increase in R, Ec and Du tends to elevate temperatures and therefore increases thickness of the thermal boundary layer. Conversely an increase in the parameters Pr decreases temperatures and reduce the thickness of thermal boundary layer.
- The nano-particle concentration magnitudes and therefore species concentration boundary layer increases with an increase of Sr , while increasing parameters Sc and Kr manifests in a reduction in nano-particle concentrations and concentration boundary layer thickness.
- Greater thickness of thermal and concentration boundary layers is achieved for $Cu - H_2O$ nanofluid relative to $Al_2O_3 - H_2O$ nanofluid.
- Both Soret and Dufour number exert, via the thermal-diffusion and diffusion-thermo cross-flow gradient effects, a significant influence on heat and mass transfer characteristics of water based nanofluids.

Future scope

The present analysis has been confined to Newtonian nanofluids. Future studies will address non-Newtonian nanofluid models such as Eringen's micropolar theory (Latiff et al. [52]), and will be communicated soon.

Acknowledgements

The authors are grateful to both reviewers for their insightful comments which have served to improve the present work.

References

1. Zaid Z, Sajid MH, Saidur R, Kamalisarvestani M and Rahim NA. Radiative properties of nanofluids. *Int. Comm. Heat Mass Transfer* 2013; 46: 74–84.
2. Sergis A, Barrett T and Hardalupas Y. Potential for improvement in high heat flux hyper vapotron element performance using nanofluids. *Proc. 24th IAEA FEC, San Diego, 2012, USA*.
3. Beg OA, Rashidi MM, Akbari M and Hosseini A. comparative numerical study of single-phase and two-phase models for Bio-nanofluid transport phenomena. *Journal of Mech. In Medicine and Biology* 2014; 14(1):1450011 (31 pages).
4. Rashidi MM, Hosseini A, Pop I, Kumar S and Freidoonimehr N. Comparative numerical study of single and two-phase models of nanofluid heat transfer in wavy channel. *Appl. Math. Mech.-Eng. Ed.* 2014; 35(7): 831-848.
5. Borbáth T, Bica D, Potencz I, Vekas L, Borbath I and Boros T. Magnetic nanofluids and magnetic composite fluids in rotating seal systems. *IOP Conference Series: Earth and Environmental Science 2010*; 12: 1-10.
6. Choi S. Enhancing thermal conductivity of fluids with nanoparticles, in *Developments and Applications of non-Newtonian flows*. *Siginer DA, Wang HP, editors, ASME* 1995; 66: 99-105.
7. Choi SUS, Zhang ZG, Yu W, Lockwood FE and Grulke EA. Anomalously thermal conductivity enhancement in nanotube suspensions. *Appl. Phys. Lett* 2001; 79: 2252.
8. Oztop HF, Rahman MM, Ahsan A, Hasanuzzaman M, Saidur R and Al-Salem KH et al. MHD natural convection in an enclosure from two semi-circular heaters on the bottom wall. *Int. J Heat Mass Transfer* 2012; 55: 1844–54.
9. Chamkha AJ and Aly AM. MHD free convection flow of a nanofluid past a vertical plate in the presence of heat generation or absorption effects. *Chem. Eng. Comm.* 2011; 198: 425-441.
10. Ellahi R. The effects of MHD and temperature dependent viscosity on the flow of non-Newtonian nanofluid in a pipe: analytical solutions. *Appl. Math. Model* 2013; 37(3): 1451–67.
11. Freidoonimehr N, Rashidi MM and Shohel MD. Unsteady MHD free convective flow past a permeable stretching vertical surface in a nanofluid. *Int. J. Thermal Sci.* 2015; 87: 136-145.
12. Sheikholeslami M, Gorji-Bandpy M, Ganji DD, Rana P and Soleimani S. Magnetohydrodynamic free convection of Al₂O₃-water nanofluid considering thermophoresis and Brownian motion effects. *Computers & Fluids* 2014; 94: 147–160.
13. Mahajan A and Arora M. Convection in rotating magnetic nanofluids. *Applied Mathematics and Computation* 2013; 219: 6284–6296.
14. Nadeem S and Saleem S. Unsteady mixed convection flow of nanofluid on a rotating cone with magnetic field. *Appl. Nanoscience* 2014; 4: 405-414.
15. Beg OA, Mabood F and Nazrul Islam M. Homotopy simulation of nonlinear unsteady rotating nanofluid flow from a spinning body. *International Journal of Engineering Mathematics* 2015; Article ID 272079, 15 pages, <http://dx.doi.org/10.1155/2015/272079>.
16. Rana P, Bhargava R and Beg O.A. Finite element simulation of unsteady magnetohydrodynamic transport phenomena on a stretching sheet in a rotating nanofluid. *Proc. I Mech. E- Part N: J. Nano materials, Nanoengineering and Nanosystems* 2013; 227: 77–99.
17. Sheikholeslami M, Hatami M and Ganji DD. Nanofluid flow and heat transfer in a rotating system in the presence of a magnetic field. *J. Molecular Liquids* 2014; 190: 112–120.

18. Hamad MAA and Pop I. Unsteady MHD free convection flow past a vertical permeable flat plate in a rotating frame of reference with constant heat source in a nanofluid. *Heat and Mass Transfer* 2011; 47: 1517–1524.
19. Ramzan M and Bilal M. Three-dimensional flow of an elastico-viscous nanofluid with chemical reaction and magnetic field effects. *J. Molecular Liquids* 2006; 200: 212–220.
20. Uddin MJ, Beg O.A and Ismail AI. Radiative convective nanofluid flow past a stretching/shrinking sheet with slip effects. *AIAA Journal of Thermo physics and Heat Transfer* 2015; 29: 513-523.
21. Rashidi MM, Momoniat E, Ferdows M and Basiri PA. Lie-group solution for free convective flow of nanofluid past a chemically reacting horizontal plate in a porous media. *Mathematical Problems in Eng.* 2014; Article ID: 239082 (21pages).
22. Turkyilmazoglu M and Pop I. Heat and mass transfer of unsteady natural convection flow of some nanofluids past a vertical infinite flat plate with radiation effect. *Int. J. Heat and Mass Transfer* 2013; 59: 167–171.
23. Satya Narayana PV, Venkateswarlu B and Venkataramana S. Thermal radiation and heat source effects on a MHD nanofluid past a vertical plate in a rotating system with porous medium. *Heat Transf Asian Res.* 2015; 44(1): 1-19.
24. Siva Reddy S and Thirupathi T. Heat and Mass transfer effects on natural convection flow in the presence of volume fraction for copper-water nanofluid. *J. Nanofluids* 2016; 5: 220-230.
25. Uddin MJ, Beg O.A., Aziz A and Ismail AI Md. Group analysis of free convection flow of a magnetic nanofluid with chemical reaction. *Mathematical Problems in Engineering* 2015; 2015, Article ID 621503, 11 pages <http://dx.doi.org/10.1155/2015/621503>.
26. Ibanez G, Lopez A, Pantoja J and Moreira J. Entropy generation analysis of a nanofluid flow in MHD porous microchannel with hydrodynamic slip and thermal radiation. *Int. J. Heat and Mass Transfer* 2016; 100: 89–97.
27. El-Kabeir SMM, Chamkha AJ, Rashad AM and Al-Mudhaf HF. Soret and Dufour effects on heat and mass transfer by Non-Darcy convection from a permeable sphere embedded in a high porosity medium with chemically reactive species. *Int. J. of Energy and Tech.* 2010; 2: 1-10.
28. Beg O.A., Prasad VR, Vasu B, Bhaskar reddy N, Li Q and Bhargava R. Free convection heat and mass transfer from an isothermal sphere to a micropolar regime with Soret/Dufour effects. *Int. J Heat and Mass Transfer* 2011; 54: 9-18.
29. Chandrasekhar B and Kishan N. Soret and Dufour effects on free convective heat and solute transfer in fluid saturated inclined porous cavity. *Eng. Sci. and Tech. Int. J.* 2015; 18: 543-554.
30. Beg O.A, Bakier AY and Prasad VR. Numerical study of free convection magnetohydrodynamic heat and mass transfer from a stretching surface to a saturated porous medium with Soret and Dufour effects. *Computational Materials Science* 2009; 46(1): 57-65.
31. Rashad A and Chamkha AJ. Heat and mass transfer by natural convection flow about truncated cone in porous media with Soret and Dufour. *Int. J. Numerical Methods for Heat & Fluid Flow* 2014; 24: 595-612.
32. Buongiorno J. Convective transport in nanofluids. *ASME J Heat Transfer* 2006; 128: 240–250.
33. Tiwari RK and Das MK. Heat transfer augmentation in a two-sided lid-driven differentially heated square cavity utilizing nanofluids. *Int. J Heat Mass Transfer* 2007; 50: 2002–2018.

34. Garoosi F, Jahanshaloo L, Rashidi MM, Badakhsh A and Ali ME. Numerical simulation of natural convection of the nanofluid in heat exchangers using a Buongiorno model. *Appl. Math. And Comp.* 2015; 254: 183-203.
35. Liron N and Wilhelm HE. Integration of the magnetohydrodynamic boundary layer equation by Meksyn's method. *J. Appl. Math. Mech. (ZAMM)* 1974; 54: 27-37.
36. Cramer KR and Pai SI. *Magnetofluid dynamics for engineers and applied physicists.* McGraw-Hill; New York, 1973.
37. Venkateswarlu B and Satya Narayana PV. Chemical reaction and radiation absorption effects on the flow and heat transfer of a nanofluid in a rotating system. *Appl. Nanoscience* 2015; 5: 351-360.
38. Ishigaki H. Periodic boundary layer near a two-dimensional stagnation point. *J. Fluid Mech.* 1970; 43: 477-486.
39. Ganapathy R. A note on oscillatory Couette flow in a rotating system. *ASME J. Appl. Mech.* 1994; 61: 208-209.
40. Das S, Jana RN and Chamkha AJ. Magnetohydrodynamic free convective boundary layer flow of nanofluids past porous plate in a rotating frame. *J. Nanofluids* 2015; 4: 176-185.
41. Oztop HF and Abu-Nada E. Numerical study of natural convection in partially heated rectangular enclosures filled with nanofluids. *Int. J. Heat Mass Transfer* 2008; 29: 1326-1336.
42. Brinkman HC. Viscosity of concentrated suspension and solution. *J. Chem. Phys.* 1952; 20: 571-581.
43. Brewster MQ. *Thermal radiative transfer properties.* Wiley: New York, 1972.
44. Beg OA, Zueco J, Takhar HS, Beg TA and Sajid A. Transient non-linear optically-thick radiative-convective double-diffusive boundary layers in a darcian porous medium adjacent to an impulsively started surface: network simulation solutions. *Comm. Nonlinear Science and Numerical Simulation.* 2009; 14: 3856-3866.
45. Beg OA, Zueco J, Beg TA, Takhar HS and Kahya E. NSM analysis of time-dependent nonlinear buoyancy-driven double-diffusive radiative convection flow in non-Darcy geological porous media. *Acta Mechanica* 2009; 202: 181-204.
46. Beg OA, Ghosh SK and Narahari M and Beg TA. Mathematical modelling of thermal radiation effects on transient gravity-driven optically-thick gray convection flow along an inclined plate with pressure gradient. *Chemical Eng. Comm.* 2011; 198: 1-15.
47. Beg OA, Zueco J, Ghosh SK and Heidari A. Unsteady magnetohydrodynamic heat transfer in a semi-infinite porous medium with thermal radiation flux: analytical and numerical study. *Advances in Numerical Analysis:* Article ID 304124, pp. 1-17, DOI: 10.1155/2011/304124.
48. Reddy JN. *An introduction to the finite element method.* 3rd ed. McGraw-Hill Book Company: New York, 2006.
49. Rana P, Bhargava R and Beg, OA. Finite element modeling of conjugate mixed convection flow of Al₂O₃-water nanofluid from an inclined slender hollow cylinder. *Physica Scripta* 2013; 88:15.
50. Greenspan HP. *The theory of rotating fluids.* Cambridge Univ. Press: UK, 2013.
51. Gebhart B. *Buoyancy-induced flows and transport.* Hemisphere: Washington, USA, 1988.
52. Latiff NAA, Uddin MJ, Beg, OA and Ismail AI. Unsteady forced bio convection slip flow of a micropolar nanofluid from a stretching/shrinking sheet. *Proc. IMECHE- Part N: J. Nanoengineering and Nanosystems* 2015; 1-11. DOI: 10.1177/1740349915613817.

TABLES

Table 1. Grid independence study for different grid sizes when $S = 0.5$

V :secondary velocity			u :primary velocity			θ : Temperature			C :Concentration		
Grid sizes											
131	151	171	131	151	171	131	151	171	131	151	171
0	0	0	0	0	0	1	1	1	1	1	1
0.1081	0.1081	0.1081	0.1278	0.1278	0.1278	0.9655	0.9655	0.9655	0.9671	0.9671	0.9671
0.1961	0.1961	0.1961	0.2354	0.2354	0.2354	0.9322	0.9322	0.9322	0.9351	0.9351	0.9351
0.2693	0.2693	0.2693	0.3278	0.3278	0.3278	0.9001	0.9001	0.9001	0.9037	0.9037	0.9037
0.3311	0.3311	0.3311	0.4082	0.4082	0.4082	0.8692	0.8692	0.8692	0.8732	0.8732	0.8732
0.3836	0.3836	0.3836	0.4789	0.4789	0.4789	0.8393	0.8393	0.8393	0.8434	0.8434	0.8434
0.4285	0.4285	0.4285	0.5413	0.5413	0.5413	0.8105	0.8105	0.8105	0.8145	0.8145	0.8145
0.467	0.467	0.467	0.5965	0.5965	0.5965	0.7827	0.7827	0.7827	0.7863	0.7863	0.7863
0.5	0.5	0.5	0.6453	0.6453	0.6453	0.7558	0.7558	0.7558	0.7589	0.7589	0.7589
0.5281	0.5281	0.5281	0.6884	0.6884	0.6884	0.73	0.73	0.73	0.7323	0.7323	0.7323

Table 2. Thermo-physical properties of water and nanoparticles

Physical properties	H_2O	Cu	Ag	Al_2O_3	TiO_2
$C_p(j/kg\ k)$	4179	385	235	765	686.2
$\rho(kg/m^3)$	997.1	8933	10500	3970	4250
$K(W/m\ k)$	0.613	401	429	40	8.9538
$\beta \times 10^{-5}(1/k)$	21	1.67	1.89	0.85	0.9
$\sigma (S/m)$	5.5×10^{-6}	59.6×10^6	62.1×10^6	35×10^6	2.6×10^6

Table 3. Comparison of Skin friction and Nusselt number for various values of Pr
($R = 0, K \rightarrow \infty, Ec = 0, Gc = 0, Sr = 0, Du = 0$)

Pr	Previous results [18]		Present results	
	C_f	Nu	C_f	Nu
0.5	2.320	5.967	2.3201221	5.9670425
1.0	2.258	6.046	2.2581991	6.0460936
1.5	2.196	6.125	2.1960249	6.1251147
2.0	2.134	6.206	2.1341135	6.2060256

Table 4. Comparison of Skin friction and Nusselt number for various values of Pr
($Gc = 0, Ec = 0, Sr = 0, Du = 0$)

Pr	Previous results [37]		Present results	
	C_f	Nu	C_f	Nu
0.5	2.3159708	5.9674	2.3159801	5.9674102
1.0	2.2567503	6.0461	2.2567602	6.0461114
1.5	2.1972895	6.1259	2.1972743	6.1259021
2.0	2.1376083	6.2066	2.1376135	6.2066035

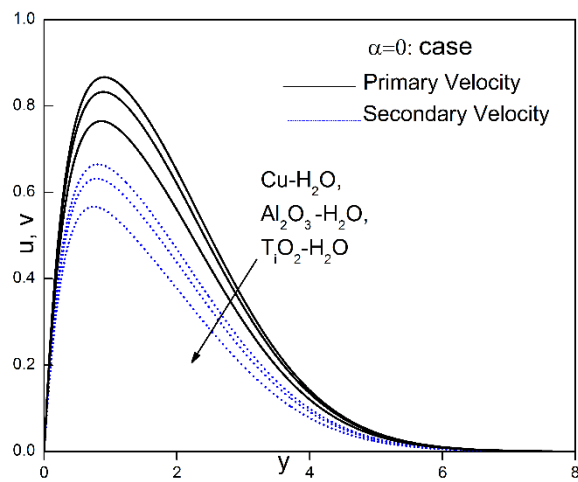


Figure 2. Velocity profiles for different nanofluids.

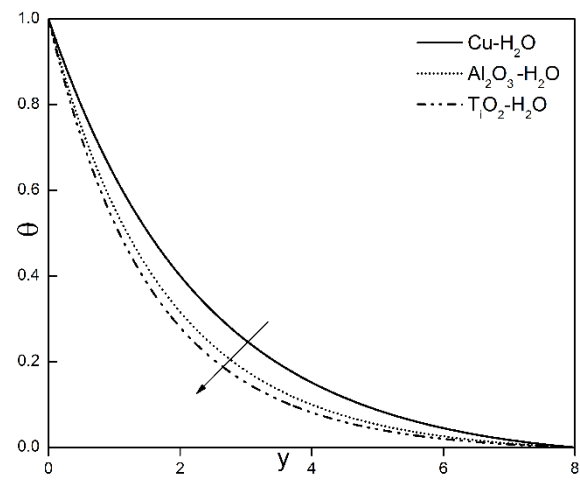


Figure 4. Temperature profiles for different nanofluids.

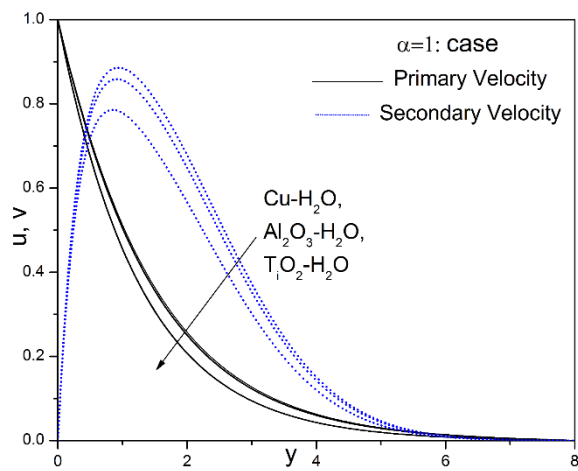


Figure 3. Velocity profiles for different nanofluids.

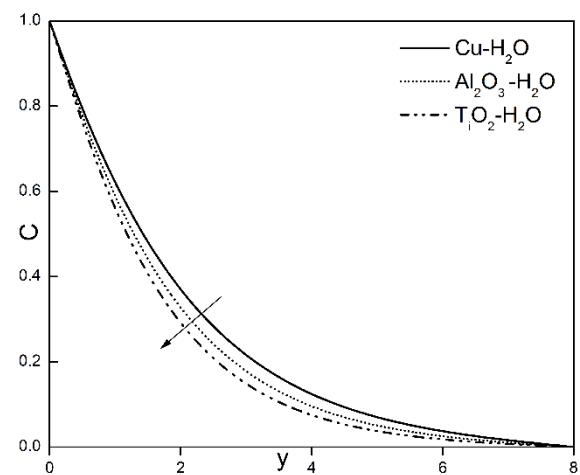


Figure 5. Concentration profiles for different nanofluids.

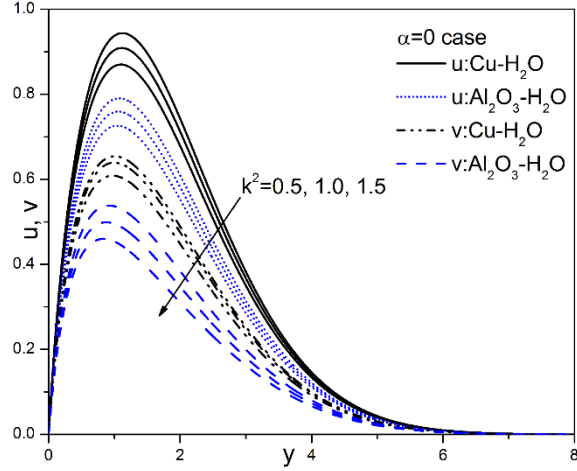


Figure 6. Velocity profiles against y for various values of Rotation parameter.

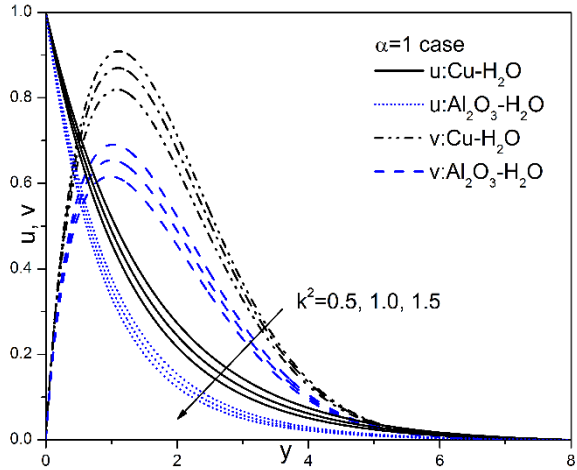


Figure 7. Velocity profiles against y for various values of Rotation parameter.

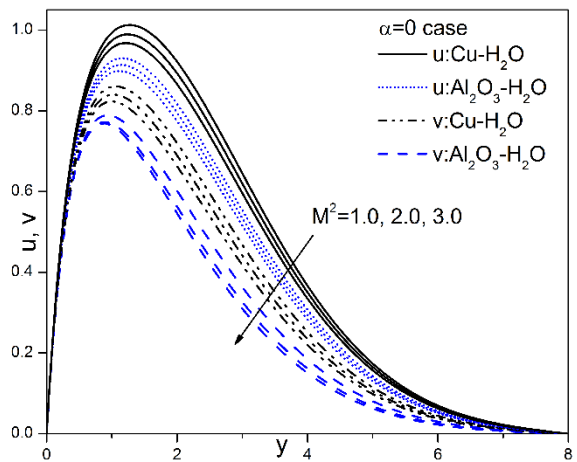


Figure 8. Velocity profiles against y for various values of Magnetic field parameter.

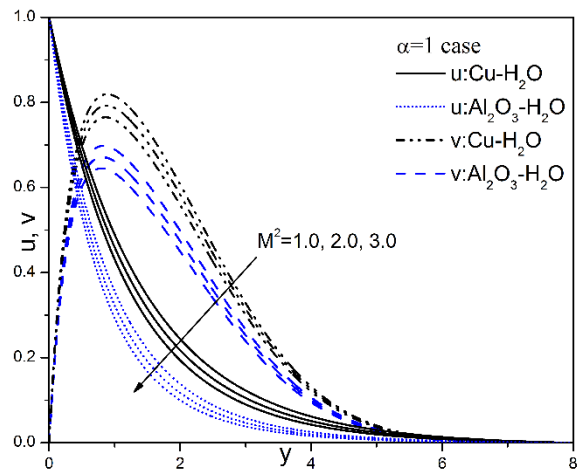


Figure 9. Velocity profiles against y for various values of Magnetic field parameter.

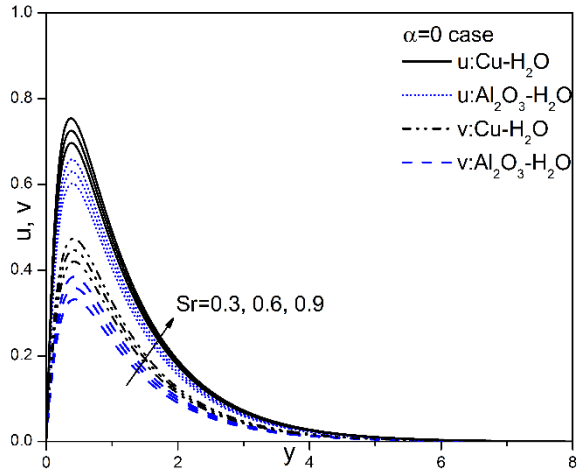


Figure 10. Velocity profiles against y for various values of Soret number.

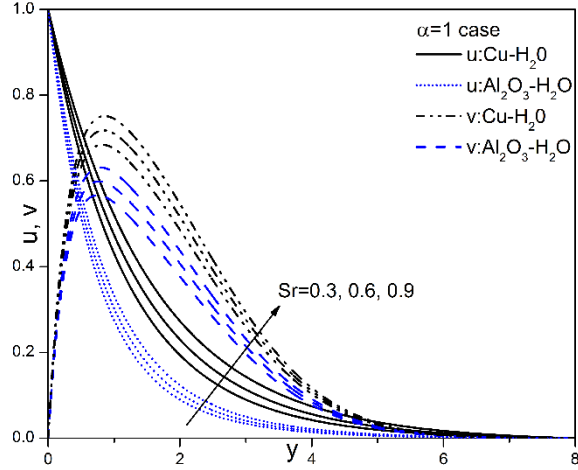


Figure 11. Velocity profiles against y for various values of Soret number.

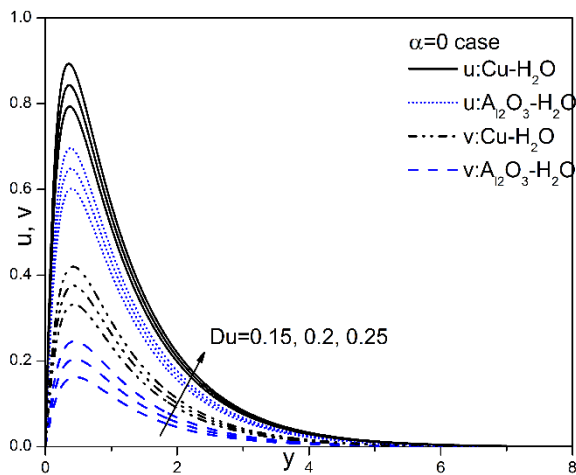


Figure 12. Velocity profiles against y for various values of Dufour number.

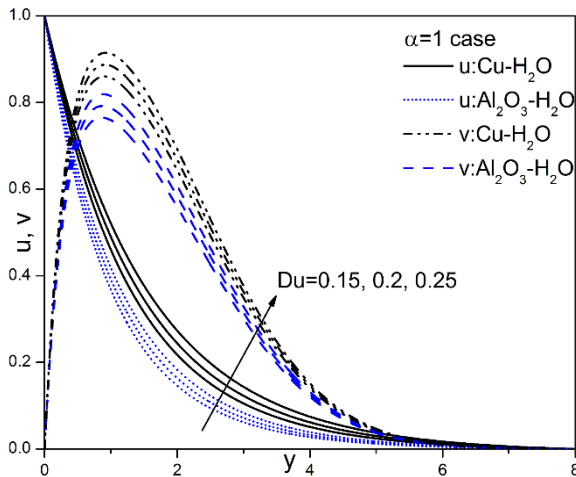


Figure 13. Velocity profiles against y for various values of Dufour number.

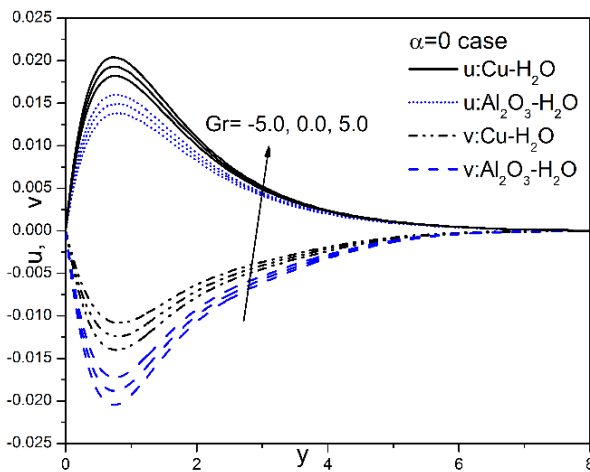


Figure 14. Velocity profiles against y for various values of thermal Grashof number.

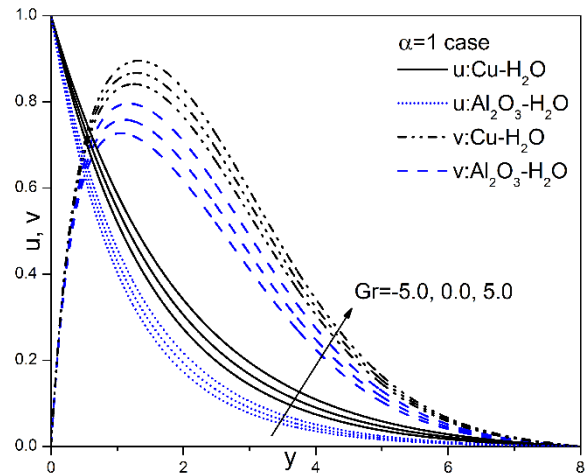


Figure 15. Velocity profiles against y for various values of thermal Grashof number.

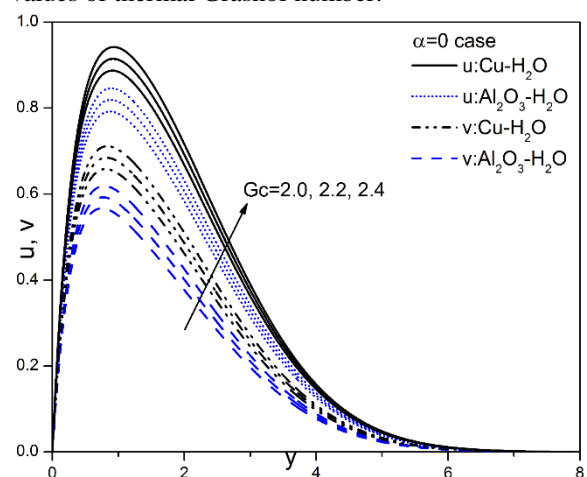


Figure 16. Velocity profiles against y for various values of solutal Grashof number.

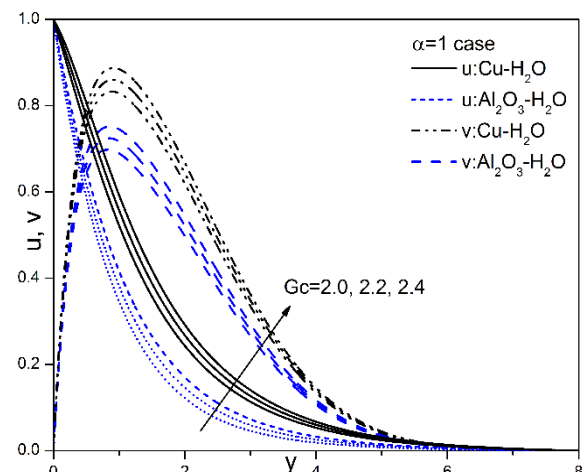


Figure 17. Velocity profiles against y for various values of solutal Grashof number.

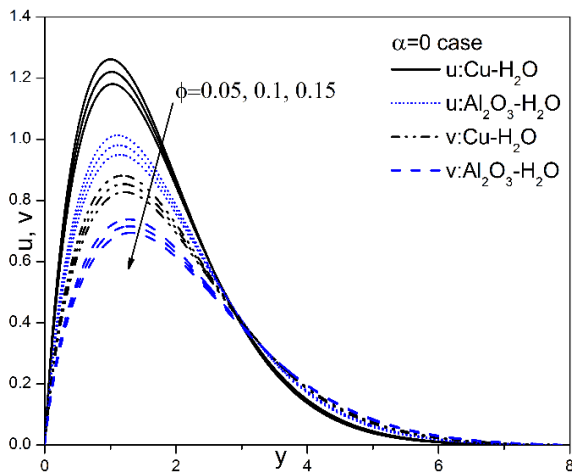


Figure 18. Velocity profiles against y for various values of volume fraction parameter.

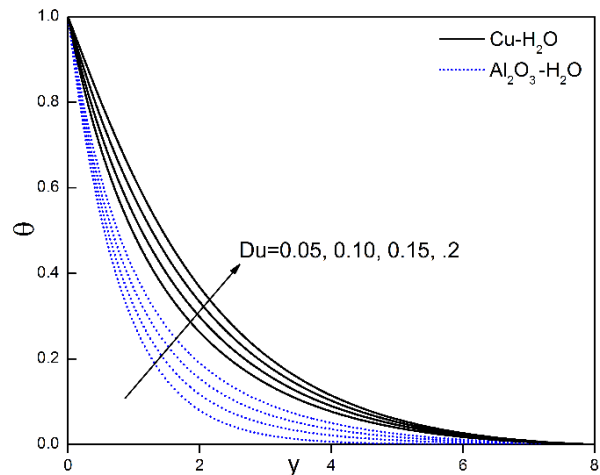


Figure 21. Temperature profiles against y for various values of Dufour number.

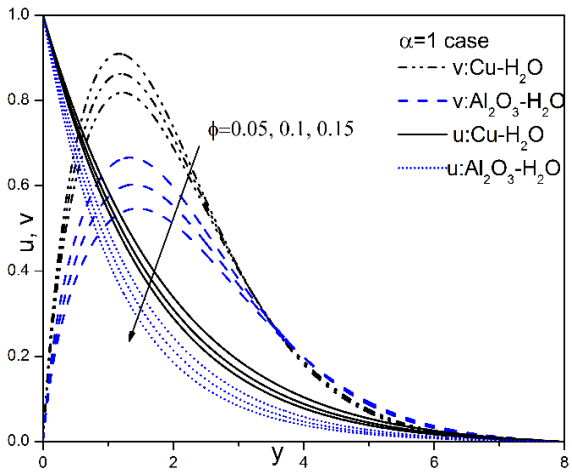


Figure 19. Velocity profiles against y for various values of volume fraction parameter.

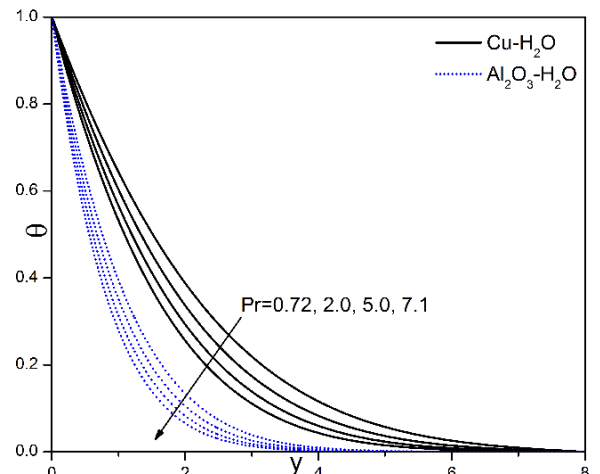


Figure 22. Temperature profiles against y for various values of Prandtl number.

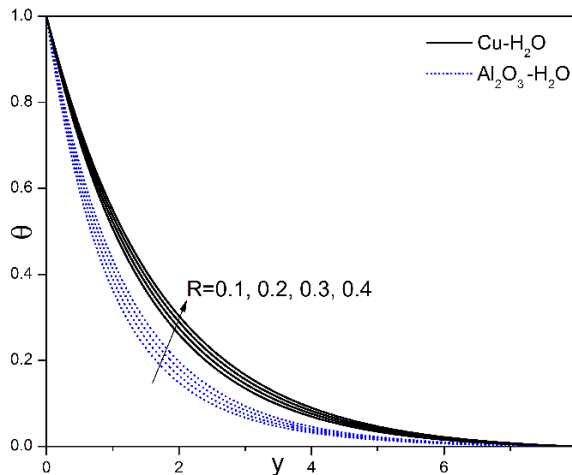


Figure 20. Temperature profiles against y for various values of radiation parameter.

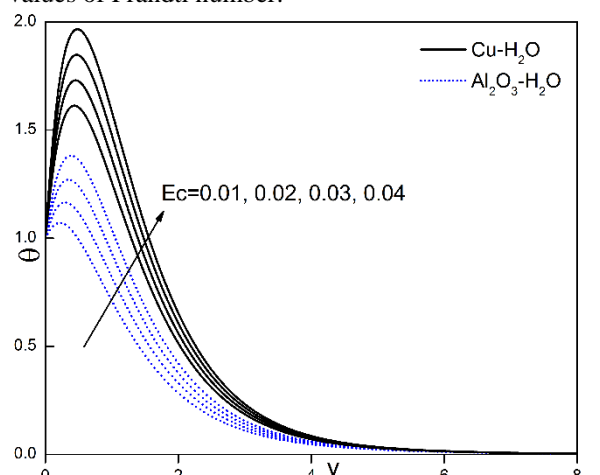


Figure 23. Temperature profiles against y for various values of Eckert number.

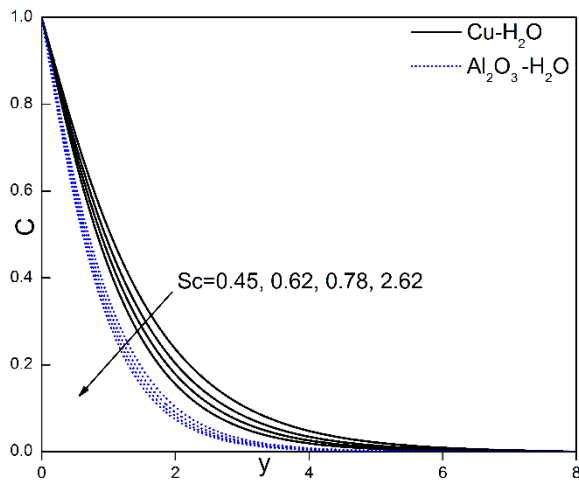


Figure 24. Concentration profiles against y for various values of Schmidt number.

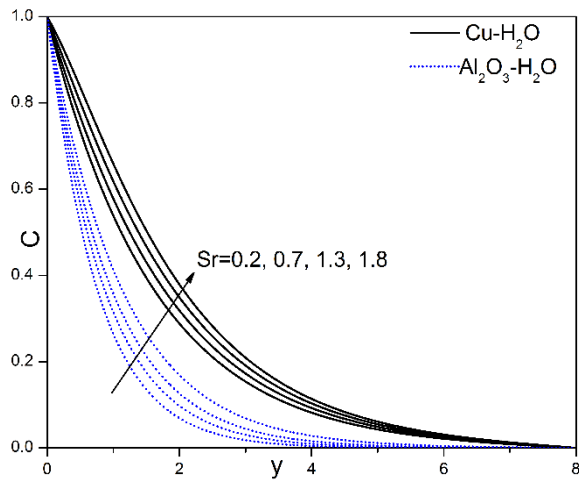


Figure 25. Concentration profiles against y for various values of Soret number.

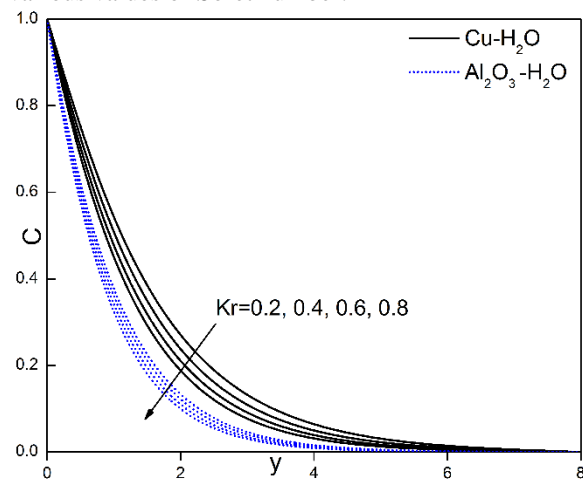


Figure 26. Concentration profiles against y for various values of chemical reaction parameter.

APPENDIX 1

Nomenclature			
(x', y', z')	Cartesian coordinates	Nu	Nusselt number
(u', v', w')	Velocities along (x', y', z') axes (ms^{-1})	C_f	Skin friction coefficient
(u, v)	Dimensionless velocities along (x', z') axes	Sh	Sherwood number
(n', t')	Constant frequency and time	K	Permeability parameter
(n, t)	Constant frequency and time	S	Suction parameter
u_0	Characteristic velocity	Greek symbols	
g	Acceleration due to gravity (ms^{-2})	Ω	Constant angular velocity (ms^{-1})
k	Permeability of porous medium	α	Constant (=0 or 1)
k^*	Mean absorption coefficient	β	Thermal expansion coefficient (K^{-1})
c_s	Concentration susceptibility	β_f	Coefficient of thermal expansion of the fluid (K^{-1})
c_p	Specific heat at constant pressure ($\text{JKg}^{-1}\text{K}^{-1}$)	β_s	Coefficient of thermal expansion of the solid (K^{-1})
k^2	Rotational parameter	ρ_f	Density of the fluid friction (Kgm^{-3})
M^2	Dimensionless magnetic field parameter	ρ_s	Density of the solid friction (Kgm^{-3})
R	Thermal radiation parameter	ρ_{nf}	Density of the nanofluid (Kgm^{-3})
Pr	Prandtl number	ν	Kinematic viscosity (m^2s^{-1})
Sr	Soret number	ν_f	Kinematic viscosity of the fluid (m^2s^{-1})
Ec	Eckert number	μ	Dynamic viscosity (Nsm^{-2})
Du	Dufour number	μ_f	Dynamic viscosity of the fluid (Nsm^{-2})
Gr	Thermal Grashof number	μ_{nf}	Viscosity of the nanofluid (Nsm^{-2})
Gc	Solutal Grashof number	σ	Electrical conductivity (Sm^{-1})
C	Non-dimensional concentration	σ_s	Electrical conductivity of the solid (Sm^{-1})
Sc	Schmidt number	σ_f	Electrical conductivity of the fluid (Sm^{-1})
Kr	Chemical reaction parameter	σ_{nf}	Electrical conductivity of the nanofluid (Sm^{-1})
Dm	Coefficient of mass diffusivity (m^2s^{-1})	σ^*	Stefan–Boltzmann constant parameter
Kt	Thermal diffusion ratio	$(\rho C_p)_{nf}$	Heat capacitance of the nanofluid ($\text{Jm}^{-3}\text{K}^{-1}$)
Tm	Mean fluid temperature	$(\rho C_p)_f$	Heat capacitance of the fluid ($\text{Jm}^{-3}\text{K}^{-1}$)
B_0	Constant applied magnetic field	ϕ	Volume fraction parameter
Ks	Thermal conductivity of the solid ($\text{Wm}^{-1}\text{K}^{-1}$)	ε	Small constant quantity
K_f	Thermal conductivity of the fluid ($\text{Wm}^{-1}\text{K}^{-1}$)	θ	Non-dimensional temperature
K_{nf}	Thermal conductivity of the nanofluid ($\text{Wm}^{-1}\text{K}^{-1}$)	Subscripts	
T'	Local temperature of the fluid (K)	f, s	Fluid, Solid
T'_w	Wall temperature of the fluid (K)	nf	Nanofluid
T'_∞	Ambient temperature of the fluid (K)	w	Condition at the wall
		∞	Condition at freestream

C'	Dimensional concentration (Kgm ⁻³)	
C'_w	Concentration at the surface (Kgm ⁻³)	
C'_∞	Concentration at freestream (Kgm ⁻³)	
w_0	Normal velocity (ms ⁻¹)	

APPENDIX 2

Variational formulation

The variational formulation associated with Eqs. (12) - (15) over a typical two-node linear element (y_e, y_{e+1}) is given by

$$\int_{y_e}^{y_{e+1}} w_1 \left[\frac{\partial u}{\partial t} - S \left(\frac{\partial u}{\partial y} \right) - A_1 \left(\frac{\partial^2 u}{\partial y^2} \right) - 2k^2 v - GrA_2 \theta - GcC + A_3 \left[M^2 + \frac{1}{K} \right] u \right] dy = 0 \quad (17)$$

$$\int_{y_e}^{y_{e+1}} w_2 \left[\frac{\partial v}{\partial t} - S \left(\frac{\partial v}{\partial y} \right) - A_1 \left(\frac{\partial^2 v}{\partial y^2} \right) + 2k^2 u + A_3 \left[M^2 + \frac{1}{K} \right] v \right] dy = 0 \quad (18)$$

$$\int_{y_e}^{y_{e+1}} w_3 \left[\frac{\partial \theta}{\partial t} - S \left(\frac{\partial \theta}{\partial y} \right) - A_4 \left(\frac{\partial^2 \theta}{\partial y^2} \right) - Du \frac{\partial^2 C}{\partial y^2} \right] dy = 0 \quad (19)$$

$$\int_{y_e}^{y_{e+1}} w_4 \left[\frac{\partial C}{\partial t} - S \left(\frac{\partial C}{\partial y} \right) - \frac{1}{Sc} \left(\frac{\partial^2 C}{\partial y^2} \right) + KrC - Sr \frac{\partial^2 \theta}{\partial y^2} \right] dy = 0 \quad (20)$$

Where w_1, w_2, w_3 and w_4 are arbitrary test functions and may be viewed as the variations in u, v, θ and C respectively. After reducing the order of integration and non-linearity, we arrive at the following system of equations.

$$\int_{y_e}^{y_{e+1}} \left[w_1 \frac{\partial u}{\partial t} - Sw_1 \left(\frac{\partial u}{\partial y} \right) + A_1 \frac{\partial w_1}{\partial y} \frac{\partial u}{\partial y} - 2k^2 w_1 v - \left[w_1 \left(\frac{\partial u}{\partial y} \right) \right]_{y_e}^{y_{e+1}} \right] dy - \left[w_1 \left(\frac{\partial u}{\partial y} \right) \right]_{y_e}^{y_{e+1}} = 0 \quad (21)$$

$$\int_{y_e}^{y_{e+1}} \left[w_2 \frac{\partial v}{\partial t} - Sw_2 \left(\frac{\partial v}{\partial y} \right) + A_1 \frac{\partial w_2}{\partial y} \frac{\partial v}{\partial y} + 2k^2 w_2 u - A_3 w_2 \left[M^2 + \frac{1}{K} \right] v \right] dy - \left[w_2 \left(\frac{\partial v}{\partial y} \right) \right]_{y_e}^{y_{e+1}} = 0 \quad (22)$$

$$\int_{y_e}^{y_{e+1}} \left[w_3 \frac{\partial \theta}{\partial t} - Sw_3 \left(\frac{\partial \theta}{\partial y} \right) + A_4 \left(\frac{\partial w_3}{\partial y} \right) \left(\frac{\partial \theta}{\partial y} \right) - \left[w_3 \left(\frac{\partial \theta}{\partial y} \right) + Duw_3 \frac{\partial C}{\partial y} \right]_{y_e}^{y_{e+1}} \right] dy - \left[w_3 \left(\frac{\partial \theta}{\partial y} \right) + Duw_3 \frac{\partial C}{\partial y} \right]_{y_e}^{y_{e+1}} = 0 \quad (23)$$

$$\int_{y_e}^{y_{e+1}} \left[w_4 \frac{\partial C}{\partial t} - Sw_4 \left(\frac{\partial C}{\partial y} \right) + \frac{1}{Sc} \left(\frac{\partial w_4}{\partial y} \right) \left(\frac{\partial C}{\partial y} \right) + Krw_4 C \right] dy - \left[w_4 \left(\frac{\partial C}{\partial y} \right) + Srw_4 \frac{\partial \theta}{\partial y} \right]_{y_e}^{y_{e+1}} = 0 \quad (24)$$

Finite Element formulation

The finite element model may be obtained from Eqs. (17) - (20) by substituting finite element approximations of the form:

$$u = \sum_{j=1}^2 u_j^e \psi_j^e, v = \sum_{j=1}^2 v_j^e \psi_j^e, \theta = \sum_{j=1}^2 \theta_j^e \psi_j^e \text{ and } C = \sum_{j=1}^2 C_j^e \psi_j^e \quad (25)$$

With $w_1 = w_2 = w_3 = w_4 = \psi_j^e$ ($i=1, 2$), where u_j^e, v_j^e, θ_j^e and C_j^e are the velocity in the direction of x -axis, y -axis and temperature respectively at the j^{th} node of typical e^{th} element (y_e, y_{e+1}) and ψ_i^e are the shape functions for this element (y_e, y_{e+1}) and are taken as:

$$\psi_1^e = \frac{y_{e+1} - y}{y_{e+1} - y_e} \text{ and } \psi_2^e = \frac{y - y_e}{y_{e+1} - y_e}, \quad y_e \leq y \leq y_{e+1} \quad (26)$$

The finite element model of the equations for e^{th} element thus formed is given by.

$$\begin{bmatrix} [K^{11}] \\ [K^{21}] \\ [K^{31}] \\ [K^{41}] \end{bmatrix} \begin{bmatrix} [K^{12}] \\ [K^{22}] \\ [K^{32}] \\ [K^{42}] \end{bmatrix} \begin{bmatrix} [K^{13}] \\ [K^{23}] \\ [K^{33}] \\ [K^{43}] \end{bmatrix} \begin{bmatrix} [K^{14}] \\ [K^{24}] \\ [K^{34}] \\ [K^{44}] \end{bmatrix} \begin{bmatrix} \{u^e\} \\ \{v^e\} \\ \{\theta^e\} \\ \{C^e\} \end{bmatrix} + \begin{bmatrix} [M^{11}] \\ [M^{21}] \\ [M^{31}] \\ [M^{41}] \end{bmatrix} \begin{bmatrix} [M^{12}] \\ [M^{22}] \\ [M^{32}] \\ [M^{42}] \end{bmatrix} \begin{bmatrix} [M^{13}] \\ [M^{23}] \\ [M^{33}] \\ [M^{43}] \end{bmatrix} \begin{bmatrix} [M^{14}] \\ [M^{24}] \\ [M^{34}] \\ [M^{44}] \end{bmatrix} \begin{bmatrix} \{u'^e\} \\ \{v'^e\} \\ \{\theta'^e\} \\ \{C'^e\} \end{bmatrix} = \begin{bmatrix} \{b^{1e}\} \\ \{b^{2e}\} \\ \{b^{3e}\} \\ \{b^{4e}\} \end{bmatrix} \quad (27)$$

Where $\{[K^{mn}], [M^{mn}]\}$ and $\{\{u^e\}, \{v^e\}, \{\theta^e\}, \{C^e\}, \{u'^e\}, \{v'^e\}, \{\theta'^e\}, \{C'^e\}\}$ and $\{b^{me}\}$ ($m, n=1, 2, 3, 4$) are the matrices of order 2×2 and 2×1 respectively and *prime* (') indicates $\frac{\partial}{\partial y}$. These matrices are defined as follows:

$$\left\{ \begin{aligned} K_{ij}^{11} &= -S \int_{y_e}^{y_{e+1}} \left[(\psi_i^e) \left(\frac{\partial \psi_j^e}{\partial y} \right) \right] dy + A_1 \int_{y_e}^{y_{e+1}} \left[\left(\frac{\partial \psi_i^e}{\partial y} \right) \left(\frac{\partial \psi_j^e}{\partial y} \right) \right] dy + A_3 \left(M^2 + \frac{1}{K} \right) \int_{y_e}^{y_{e+1}} [(\psi_i^e)(\psi_j^e)] dy, \\ K_{ij}^{12} &= -2k^2 \int_{y_e}^{y_{e+1}} (\psi_i^e)(\psi_j^e) dy, K_{ij}^{13} = -GrA_2 \int_{y_e}^{y_{e+1}} (\psi_i^e)(\psi_j^e) dy, K_{ij}^{14} = -GcA_2 \int_{y_e}^{y_{e+1}} (\psi_i^e)(\psi_j^e) dy, \\ M_{ij}^{11} &= \int_{y_e}^{y_{e+1}} (\psi_i^e)(\psi_j^e) dy, M_{ij}^{12} = M_{ij}^{13} = M_{ij}^{14} = 0, \\ K_{ij}^{22} &= -S \int_{y_e}^{y_{e+1}} \left[(\psi_i^e) \left(\frac{\partial \psi_j^e}{\partial y} \right) \right] dy + A_1 \int_{y_e}^{y_{e+1}} \left[\left(\frac{\partial \psi_i^e}{\partial y} \right) \left(\frac{\partial \psi_j^e}{\partial y} \right) \right] dy + A_3 \left(M^2 + \frac{1}{K} \right) \int_{y_e}^{y_{e+1}} [(\psi_i^e)(\psi_j^e)] dy, \\ K_{ij}^{21} &= 2k^2 \int_{y_e}^{y_{e+1}} (\psi_i^e)(\psi_j^e) dy, K_{ij}^{23} = 0, K_{ij}^{24} = 0 \\ M_{ij}^{22} &= \int_{y_e}^{y_{e+1}} (\psi_i^e)(\psi_j^e) dy, M_{ij}^{21} = M_{ij}^{23} = 0, \end{aligned} \right.$$

$$\left\{ \begin{array}{l}
K_{ij}^{31} = 0, K_{ij}^{32} = 0, \\
K_{ij}^{33} = -S \int_{y_e}^{y_{e+1}} \left(\psi_i^e \right) \left(\frac{\partial \psi_j^e}{\partial y} \right) dy + A_4 \int_{y_e}^{y_{e+1}} \left[\left(\frac{\partial \psi_i^e}{\partial y} \right) \left(\frac{\partial \psi_j^e}{\partial y} \right) \right] dy, K_{ij}^{34} = -Du \int_{y_e}^{y_{e+1}} \left(\psi_i^e \right) \left(\frac{\partial \bar{u}}{\partial y} \right) \left(\frac{\partial \psi_j^e}{\partial y} \right) dy, \\
M_{ij}^{31} = 0, M_{ij}^{32} = 0, M_{ij}^{33} = \int_{y_e}^{y_{e+1}} \left(\psi_i^e \right) \left(\psi_j^e \right) dy, M_{ij}^{34} = 0 \\
K_{ij}^{41} = 0, K_{ij}^{42} = 0, K_{ij}^{43} = -Sr \int_{y_e}^{y_{e+1}} \left(\psi_i^e \right) \left(\frac{\partial \psi_i^e}{\partial y} \right) \left(\frac{\partial \psi_j^e}{\partial y} \right) dy, \\
K_{ij}^{44} = -S \int_{y_e}^{y_{e+1}} \left[\left(\psi_i^e \right) \left(\frac{\partial \psi_j^e}{\partial y} \right) \right] dy + \frac{1}{Sc} \int_{y_e}^{y_{e+1}} \left[\left(\frac{\partial \psi_i^e}{\partial y} \right) \left(\frac{\partial \psi_j^e}{\partial y} \right) \right] dy + Kr \int_{y_e}^{y_{e+1}} \left(\psi_i^e \right) \left(\psi_j^e \right) dy, \\
M_{ij}^{41} = 0, M_{ij}^{42} = 0, M_{ij}^{44} = \int_{y_e}^{y_{e+1}} \left(\psi_i^e \right) \left(\psi_j^e \right) dy, M_{ij}^{43} = 0 \\
b_i^{1e} = \left[\left(\psi_i^e \right) \left(\frac{\partial u}{\partial y} \right) \right]_{y_e}^{y_{e+1}}, b_i^{2e} = \left[\left(\psi_i^e \right) \left(\frac{\partial v}{\partial y} \right) \right]_{y_e}^{y_{e+1}}, \\
b_i^{3e} = \left[\left(\psi_i^e \right) \left(\frac{\partial \theta}{\partial y} \right) + Du \left(\psi_i^e \right) \left(\frac{\partial C}{\partial y} \right) \right]_{y_e}^{y_{e+1}}, b_i^{4e} = \left[\left(\psi_i^e \right) \left(\frac{\partial C}{\partial y} \right) + Sr \left(\psi_i^e \right) \left(\frac{\partial \theta}{\partial y} \right) \right]_{y_e}^{y_{e+1}}
\end{array} \right.$$